J. Fluid Mech. (2010), *vol.* 660, *pp.* 162–196.
doi:10.1017/S0022112010002612

Short- to long-wave resonance and soliton formation in boundary-layer interaction with a liquid film

M. VLACHOMITROU AND N. PELEKASIS†

Department of Mechanical & Industrial Engineering, University of Thessaly, Leoforos Athinon, Pedion Areos, 38834 Volos, Greece

(Received 29 June 2009; revised 2 May 2010; accepted 3 May 2010; first published online 12 July 2010)

Dynamic interaction between a boundary layer of air and a liquid film is investigated in this paper. The low air-to-film-viscosity ratio is considered in which case the boundary layer is quasi-steady on the time scale within which interfacial waves develop. The base flow consists of a boundary layer that drags a film of constant shear. Linear analysis, in the context of triple-deck theory, predicts the formation of a wavepacket of capillary waves that advances and spreads with time. The Froude number of de-/anti-icing fluids or water interacting with air falls well within the supercritical regime, i.e. $Fr > Fr_{Cr}$. Numerical simulations of such flow systems were performed in the context of triple-deck theory, and they do not exhibit wave saturation or formation of uniform wavetrains. The long-term interaction is mainly dependent on film inertia as this is characterized by parameter $\mathfrak{M} = (\mu/\mu_f)^2(\rho_f/\rho)$, which involves film and air viscosity and density ratios, and the dimensionless film thickness, H_0, and shear, λ, provided by the base flow. Weakly nonlinear analysis taking into consideration mean drift, i.e. generation of long waves, due to self-interaction of the linear wave to $O(\varepsilon^2)$ in amplitude of the initial disturbance, reveals resonance between the wavepacket predicted by linear theory and long waves when the group velocity of the former happens to coincide with the phase velocity, $H_0\lambda$, of long interfacial waves. Numerical simulations with anti-icing fluids and water verify this pattern. In both cases, long waves eventually dominate the dynamics and, as they are modulated with time, they lead to soliton-type structures. Anti-icing fluids eventually exhibit oscillatory spikes whose mean value never exceeds $2H_0$, roughly. Water films exhibit a single spike that keeps growing, thus generating a large separation bubble.

Key words: boundary-layer structure, interfacial flows (free surface), solitary waves

1. Introduction

We examine the nonlinear behaviour of interfacial waves that develop when a subsonic laminar gas boundary layer interacts with a thin liquid film. Gas–liquid interaction at high Reynolds number, *Re*, is presumed by many researchers to be of central importance in airfoil performance under rainfall conditions or during application of de-/anti-icing fluids. Bezos *et al.* (1992) reported that the interaction of the boundary layer with the liquid film is responsible for changes in the effective

† Email address for correspondence: pel@uth.gr

camber of the airfoil, which negatively affects the airfoil performance within the entire range of realizable angles of attack. Similarly, experiments that were performed on commercial airfoils sprayed with anti-icing fluids (Hill & Zierten 1993) showed that such fluids remain on the airfoil surface until well after take-off and that they are the source of adverse aerodynamic effects, especially at large angles of attack.

There is limited experimental work available focusing on the development of interfacial waves in the flow arrangement under investigation, especially in the nonlinear regime. Nevertheless, relevant experimental measurements and preliminary stability-analysis results were reported by Craik (1966) for the case of channel flow interacting with a thin liquid film that grows on the lower flat wall. He was able to capture a different kind of instability that does not appear when thicker films are present. More specifically, he noticed that when the liquid film is thick, periodic waves appear. These waves, which Craik refers to as 'fast' waves, are sinusoidal and their speed is greater than the velocity of the interface. On the contrary, for thinner films (0.0128–0.0307 cm) Craik observed non-periodic waves that have steep spikes and move with velocity smaller than the velocity of the interface ('slow' waves). In cases where the liquid's thickness is even smaller, he captured the formation of 'dry' regions on the solid surface. Ludwieg & Hornung (1989), using a simple visualization technique, captured interfacial waves and their effect in transition for boundary-layer interaction with an oil film. They also performed stability analysis which, in agreement with the subsequent linear-stability results in the context of the triple-deck theory by Timoshin (1997), verified that the interfacial waves that they observed essentially correspond to the most strongly amplified wave predicted by the stability analysis. Finally, Ozgen, Carbonaro & Sarma (2002) used different de-/anti-icing fluids deposited on the lower wall of a wind tunnel that was sheared by a turbulent airflow. The above researchers tried to determine the characteristics of the observed waves by using a light-absorption technique and compared them with linear theory. They observed periodic waves with velocities greater than the velocity of the interface, but for thinner films, they captured non-periodic waves as well as dry regions.

As far as the evolution of interfacial waves is concerned, linear stability analysis is typically used to provide the dominant wavenumbers and their growth rates depending on the flow parameters, namely Reynolds, Weber and Froude numbers as well as density and viscosity ratios. The Orr–Sommerfeld stability equations are commonly employed in the context of channel, e.g. Craik (1966) and Yiantsios & Higgins (1988), or boundary-layer flows, e.g. Ludwieg & Hornung (1989) and Ozgen *et al.* (1998). The main findings of this line of research are the dominance of Tolmien–Schlichting waves as far as growth rates are concerned and the shorter wavelengths associated with interfacial waves, especially for large film-to-gas-viscosity ratio. Assuming a quasi-laminary approach in his stability analysis, Craik (1966) identified the role of tangential stress in destabilizing capillary waves for a wide range of air stream velocities, provided the water film remains sufficiently thin. Stability analysis based on the triple-deck theory (Timoshin 1997; Pelekasis & Tsamopoulos 2001) verifies the importance of interfacial waves in the limit of large free-stream Reynolds numbers, even though their growth rate is lower than that of the Tollmien–Schlichting (T–S) waves. In addition, it was shown by Pelekasis & Tsamopoulos (2001) that interfacial waves are absolutely unstable within a parameter range that is relevant to the case of high-Re flow above a thin water film. Therefore, it was suggested that the liquid film that covers an airfoil may be responsible for reduction of the lift coefficient, possibly through premature boundary-layer separation as a result of their interaction.

It is, however, important to ascertain the persistence of the above phenomena in the nonlinear regime of the present study.

A recent numerical study by Vlachomitrou & Pelekasis (2009) based on the nonlinear triple-deck formulation, hereinafter referred to as I, revealed the formation of spikes during growth of interfacial waves, leading to solitons with height that varies significantly depending on film inertia. The latter is determined by parameter $\mathfrak{M} = (\mu/\mu_w)^2 \rho_w/\rho$. In addition, it was shown that for viscous films ($\mu/\mu_w \ll 1$), T–S waves grow on a much faster time scale than interfacial waves and that the flow in the gas phase is quasi-steady on the time scale within which interfacial waves grow.

Most of the relevant studies focus on the linear regime of wave growth. Comparisons against theoretical predictions are also mostly restricted to linear stability analysis. In this study, an effort is made to interpretavailable experimental and numerically obtained results in the context of weakly nonlinear and nonlinear theories. To this end, we focus on the evolution of interfacial waves that develop when a gas boundary layer interacts with a thin liquid film, i.e. water or anti-icing fluids. Due to very disparate time scales governing the development of interfacial and T–S waves, we assume that all changes in the gas phase occur solely as a result of changes in the shape of the interface. Thus, we treat the gas phase as quasi-steady. This is a well-justified assumption for systems characterized by negligibly small viscosity ratio, as is the case with films consisting of water or de-/anti-icing fluids, which essentially allows us to decouple the development of interfacial waves from that of T–S waves. In this fashion the evolution of interfacial waves is studied at large times and/or relatively large amplitudes of the initial disturbance. Subsequently, an effort is made to predict the behaviour of growing waves based on linear and weakly nonlinear analyses. The governing equations describing the nonlinear triple-deck formulation of the problem for air–water or air–de-/anti-icing fluid interaction are provided in § 2. In this framework, and as far as the linear regime is concerned, nonlinear simulations for the air–water and the air–deicing fluid systems performed in I indicate that linear stability analysis (Pelekasis & Tsamopoulos 2001) adequately describes the evolution of the unstable wavepacket over a certain time interval. Elements of the linear stability analysis for the air–film systems studied herein, as well as the methodology used to obtain the relevant group velocities of the unstable wavepacket are provided in § 3.1.

The possibility for steady travelling waves is also of interest near and beyond the critical region, in terms of the Froude number, where interfacial waves first become unstable. Such a possibility was shown by Blennerhassett (1980) for stratified Poiseuille and Couette flow in a channel, by resorting to the nonlinear Schrödinger equation describing the evolution of linearly unstable waves near criticality. It should be stressed, however, that due to the very large critical Reynolds numbers obtained with increasing critical wavenumber as the thickness ratio between the top and bottom layers increased, numerical evaluation of the Schrödinger constants in that parameter range was rather ambiguous. Since the triple-deck approach is valid as Reynolds number becomes very large, regions near the film–air interface are accurately resolved numerically while Reynolds number is eliminated from the problem parameter set.

However, mode saturation and a steady travelling wave with the characteristics provided by linear stability analysis, $E = \exp(\mathrm{i}(kX - \omega_r T))$, with k and ω_r denoting the wavenumber and frequency of the unstable mode, was never observed in the nonlinear simulations performed in I even for values of the Froude number near criticality. Simulations presented in I pertaining to films of anti-icing fluids or water interacting with a boundary layer, i.e. when $Fr > Fr_{Cr}$, revealed long-wave formation as a precursor to solitons. The latter waveforms exhibited oscillatory maximum height

in the case of anti-icing fluids, in the manner predicted by Djordjevic & Redekopp (1977) and Ma & Redekopp (1979) as a result of short- to long-wave resonance for capillary Stokes waves. In order to obtain insight regarding growth of unstable modes near criticality as well as mode interaction and resonance, the nonlinear Schrödinger equation is derived for the case with negligible film inertia. This flow situation pertains to the air–de-/anti-icing fluid system and is easier to handle analytically via the multiple-time-scale method. This approach will provide the underlying mechanism behind the phenomena observed in I as well as in certain experimental observations, e.g. Craik (1966). In the case of water films, the soliton-type structure that was captured assumed the form of a single growing spike that exhibited unlimited growth, cusp formation and eventually a singularity in the pressure gradient.

A singular behaviour of the latter type was predicted by Brotherton-Ratcliffe & Smith (1987) and Smith (1988) in nonlinear studies on the dynamics of boundary layers over surface distortions, and was identified as a finite-time singularity of the triple-deck formulation. In fact, the importance of Schroedinger's equation in the early stages of nonlinear development of high-frequency T–S disturbances in a boundary layer was first recognized by Smith & Burggraf (1985) and Smith (1986), where it was also pointed out that sideband instabilities did not occur. Such high-frequency disturbances also dominate in the present study as Fr increases beyond criticality. In the above studies it was also shown that the long-time behaviour is controlled by spikes whose evolution is governed by the Benjamin–Ono equation. This is essentially the Euler equation for the displacement thickness with an integral term substituted for the pressure gradient. More recently, in Kachanov, Ryzhov & Smith (1993) and Li *et al.* (1998), it was shown that the Benjamin–Ono equation is associated with solitary-wave interaction with evolving wavepackets, spike-soliton formation and the initial stage of vorticity bursts and transition in boundary layers. These associations were corroborated by experimental observations by Kachanov *et al.* (1993). Furthermore, they were seen to persist and play a key role in the later development of three-dimensional disturbances.

In order to assess the possibility for similar type of interactions leading to mean-flow generation in the context of interfacial wave growth studied herein, i.e. evolution of the long-wave component of the initial disturbance, mode interaction leading to the E° component is accounted for and a Davey & Stewartson-type set of equations is derived (Davey & Stewartson 1974) in § 3.2:

$$f = \sum_{n=1}^{\infty} \varepsilon^n f_n, \quad f_n = \sum_{m=0}^{n} f_{n,m}(\tau, \zeta) E^m + \text{c.c.}, \quad f_{1,0} = 0, \quad f_{1,1} \equiv d, \tag{1.1}$$

$$\frac{\partial d}{\partial \tau} + S_1 \frac{\partial^2 d}{\partial \zeta^2} = S_2 d + S_3 d|d|^2 + S_4 f_{20} d, \tag{1.2}$$

$$(H_0 \lambda - c_G) \frac{\partial f_{2,0}}{\partial \tau} = S_5 \frac{\partial |d|^2}{\partial \zeta}. \tag{1.3}$$

In the above equations ε is a measure of the amplitude of the primary interfacial wave, $f_{2,0}$ the mean-flow component of the interface obtained to second order in the amplitude and S_1, S_2, S_3, S_4 and S_5 are complex constants obtained in § 3.2; H_0, λ denote the dimensionless base flow film thickness and shear stress exerted on the film by the surrounding boundary layer. When mean-flow development is neglected the above set of equations is recast into the nonlinear Schrödinger equation. We follow the work of Djordjevic & Redekopp (1977), who studied the motion of a

two-dimensional packet of capillary–gravity waves on water of finite depth. They examined the stability of the Stokes capillary–gravity wavetrain and identified a resonant interaction between a capillary–gravity wave and a long gravity wave. Resonance takes place when the group speed of the capillary wave matches the phase velocity of a shallow-water gravity wave. In the same study they showed that the long-wave component is generated by the self-interaction of the short wave. In this study we investigate whether such a behaviour is present in the flow under consideration. It should be stressed that even though the analysis presented here is not strictly valid for the case of air–water interaction, due to film inertia, nevertheless the mechanism identified for the case of de-/anti-icing fluids is also quite useful in explaining growth of water films.

In §§ 4.1 and 4.2 numerical results are presented for the two fluid systems of interest. The appearance of finite-time singularities (Smith 1988), front formation (Saarlos & Hohenberg 1992; Couairon & Chomaz 1997) as well as the appearance of spike solitons (Kachanov *et al.* 1993; Li *et al.* 1998) are discussed and interpreted in the context of short- to long-wave resonance. Finally, conclusions are drawn in § 5 regarding the dominant mechanism behind spike formation in interfacial waves, based on the findings of weakly nonlinear and numerical analyses.

2. Problem formulation

2.1. *Base flow*

We consider a thin liquid film of density ρ_w and viscosity μ_w that covers a flat plate of characteristic length L. Above the film flows a gas stream of density ρ, viscosity μ and free stream velocity U_∞, $Re = U_\infty \rho L/\mu \gg 1$, which puts the film into motion. The equations that describe the basic flow have been calculated numerically as well as asymptotically (Smyrnaios, Pelekasis & Tsamopoulos 2000). In the limit $H_f/(LRe^{-1/2}) \to 0$, where H_f is the film thickness and $LRe^{-1/2}$ the thickness of the boundary layer, the solution inside the boundary layer assumes the Blasius profile. The shear rate exerted on the liquid film, as predicted based on the Blasius solution evaluated on the interface, is $\lambda = (\partial U_0/\partial Y')(x, Y' = 0) \approx (0.332/\sqrt{x})$, $Y' = y'/(LRe^{-1/2})$. Inside the liquid film the thickness and the velocity are

$$H_o(x) = x^{3/4}\sqrt{\frac{2}{0.332}}, \quad u_o(x, y) = x^{1/4} z \sqrt{0.664}, \quad z = \frac{y}{H_0(x)}, \tag{2.1a}$$

$$H_o(x) = x^{1/4}\sqrt{\frac{2}{0.332}}, \quad u_o(x, y) = x^{-1/4} z \sqrt{0.664}, \quad z = \frac{y}{H_0(x)}, \tag{2.1b}$$

when a constant rainfall (Smyrnaios *et al.* 2000) or a constant mass-flow rate (Timoshin 1997) is assumed, respectively. The characteristic scales that have been used in the gas phase are L and $LRe^{-1/2}$ as characteristic length scales in the x and y directions, respectively, and U_∞ and $U_\infty Re^{-1/2}$ as characteristic velocities in the x and y directions, respectively. In the liquid film, L and H_f have been used as characteristic length scales in the x and y directions, and u_f and $u_f H_f/L$ as characteristic velocities in the x and y directions, respectively. Relevant estimates of H_f and u_f are provided in Smyrnaios *et al.* (2000) and Nelson, Alving & Joseph (1995) for the case of a steady rainfall rate, $\dot{r}$, and a constant mass-flow rate, Q, respectively, based on the mass balance and shear stress balances written on the gas–liquid interface.

2.2. *Governing equations*

We are interested in examining the nonlinear evolution of interfacial waves that appear when airflow interacts with a thin liquid film. Assuming that the liquid film is much more viscous than the gas we consider the limit $\mu/\mu_w \to 0$. In this limit interfacial waves evolve much slower than T–S waves, and therefore, a quasi-stationary state is assumed in the gas phase.

Dimensionless quantities are introduced via the triple-deck characteristic scales (Timoshin 1997; Pelekasis & Tsamopoulos 2001): length $\ell = LRe^{-3/8}$ in the streamwise direction and thickness $LRe^{-5/8}$ in the perpendicular direction for both the gas stream and the film. The film thickness as estimated by the base flow (Smyrnaios *et al.* 2000) is indeed of the order $H_f = LRe^{-5/8}$. The characteristic velocities in the gas phase are δU_∞ in the streamwise direction and $\delta^3 U_\infty$ in the perpendicular direction, where $\delta = Re^{-1/8}$, whereas in the liquid phase, the characteristic velocities are $u_f = (\mu/\mu_w)\delta U_\infty$ and $(\mu/\mu_w)\delta^3 U_\infty$ in the streamwise and perpendicular directions, respectively. The quantity $\delta^2 \rho U_\infty^2$ is used as a pressure scale for both phases. The above scales are obtained as a result of balancing inertia, and viscous and pressure terms in the lower deck. Finally, the time scale appropriate for the development of interfacial waves, $\hat{T} = \ell/u_f = \ell/(\delta(\mu/\mu_w)U_\infty)$, is introduced in order to make time dimensionless.

In the gas phase we use the transformed variable $\overline{Y} = Y - H(X, T)$, where H is the film thickness and X a local longitudinal coordinate around x_0, $X = (x - x_0)/Re^{-3/8}$. Moreover, we introduce Prandtl's transposition via the variable $\overline{V}$, where $\overline{V} = V - U(\partial H/\partial X) - (\mu/\mu_w)(\partial H/\partial T)$. Therefore, the dimensionless equations that describe the flow in the viscous sublayer of the boundary layer are as follows:

X-momentum:

$$\frac{\mu}{\mu_w}\frac{\partial U}{\partial T} + U\frac{\partial U}{\partial X} + \overline{V}\frac{\partial U}{\partial \overline{Y}} = -\frac{\partial P}{\partial X} + \frac{\partial^2 U}{\partial \overline{Y}^2} \quad \text{or} \quad \frac{\mu}{\mu_w}\frac{\partial U}{\partial T} + U\frac{\partial U}{\partial X} - \frac{\partial \Psi}{\partial X}\frac{\partial U}{\partial \overline{Y}} = -\frac{\partial P}{\partial X} + \frac{\partial^2 U}{\partial \overline{Y}^2}, \tag{2.2a, b}$$

where $U = \partial\Psi/\partial\overline{Y}$ is the longitudinal velocity component. Since this study focuses on the evolution of interfacial waves in a passive gas phase (see simulations in I), the time derivatives in the x-momentum are dropped. Y-momentum establishes the pressure as being independent of the transverse direction:

$$\frac{\partial P}{\partial \overline{Y}} = 0. \tag{2.3}$$

The pressure is related to the displacement thickness by the interaction law. This law emerges from the solution of Laplace's equation in the upper deck of the boundary layer:

$$P = \frac{1}{\pi}\int_{-\infty}^{+\infty} \frac{\partial A}{\partial s}\frac{\mathrm{d}s}{x - s}. \tag{2.4}$$

Continuity of velocity between the main and upper deck gives

$$U(\overline{Y} \to \infty) = \lambda(A(X) + \overline{Y} + H - H_0), \tag{2.5}$$

where $\lambda = \partial U_0/\partial Y'$ $(x, Y' = 0)$ and H_0 refers to the dimensionless shear rate on the flat plate and the film thickness, as predicted by the base solution.

In the liquid film we introduce the transformed variable $\overline{\overline{y}} = y/H(X, T)$ along with the triple-deck length and time scales. Thus, conditions on the gas–liquid interface,

$\overline{Y}=0$, $\overline{\overline{y}}=1$, read as follows:

Continuity of tangential and normal velocities:

$$U=\frac{\mu}{\mu_w}u, \quad \left.\frac{\partial \Psi}{\partial X}\right|_{\overline{Y}}=0, \tag{2.6a,b}$$

continuity of tangential and normal stresses:

$$\frac{\partial U}{\partial \overline{Y}}=\frac{1}{H}\frac{\partial u}{\partial \overline{\overline{y}}}, \quad P-p=\frac{1}{We}\frac{\partial^2 H}{\partial X^2}, \tag{2.7a,b}$$

and the kinematic boundary condition:

$$\frac{\partial H}{\partial T}+\frac{\partial \psi}{\partial X}=0. \tag{2.8}$$

Upper- and lower-case letters denote quantities defined in the gas phase and the film, respectively.

In the x-momentum inside the film we substitute the normal-force balance (cf. (2.7b)) for the liquid pressure. Thus, the governing equations in the film are as follows:

X-momentum:

$$\mathfrak{M}\left(\frac{\partial u}{\partial T}+u\frac{\partial u}{\partial X}+\frac{\overline{\overline{y}}-1}{H}\frac{\partial u}{\partial \overline{\overline{y}}}\frac{\partial \psi}{\partial X}\right)=-\frac{\partial P}{\partial X}+\frac{1}{We}\frac{\partial^3 H}{\partial X^3}-\frac{1}{Fr}\frac{\partial H}{\partial X}+\frac{1}{H^2}\frac{\partial^2 u}{\partial \overline{\overline{y}}^2}, \tag{2.9}$$

where ψ is the stream function in the film with $u=(1/H)(\partial\psi/\partial\overline{\overline{y}})$.

y-momentum:

$$\frac{\partial p}{\partial \overline{\overline{y}}}=0, \tag{2.10}$$

and the non-slip, non-penetration conditions on the surface of the flat plate:

$$\overline{\overline{y}}=0: \quad u=\psi=0. \tag{2.11}$$

The following parameters determine the importance of inertia, surface tension and gravitational forces, respectively, in the film motion: $\mathfrak{M}=(\mu/\mu_w)^2(\rho_w/\rho)$, $1/We=(\mu/\mu_w)^2(\delta^4\sigma/\rho u_f^2 H_f)$, $1/Fr=((\rho_w/\rho)-1)(\mu/\mu_w)^2(gH_f/u_f^2)$.

In the special case where $\mathfrak{M}\to 0$, the resulting equation that describes flow in the liquid film does not include inertia terms and a simple derivation provides the spatio-temporal evolution of the interface as a result of shear, pressure, surface tension and gravity forces:

$$\frac{\partial H}{\partial T}=-\frac{\partial}{\partial X}\left(\frac{H^2}{2}\left.\frac{\partial U}{\partial \overline{Y}}\right|_{\overline{Y}=0}\right)+\frac{\partial}{\partial X}\left(\frac{H^3}{3}\frac{\partial P}{\partial X}\right)-\frac{\partial}{\partial X}\left(\frac{H^3}{3We}\frac{\partial^3 H}{\partial X^3}\right)+\frac{\partial}{\partial X}\left(\frac{H^3}{3}\frac{1}{Fr}\frac{\partial H}{\partial X}\right). \tag{2.12}$$

The above equation is used in place of (2.6)–(2.11) and pertains mostly to the interaction of anti-icing fluids with an oncoming boundary layer of air, due to the very large viscosity of the former.

In all cases we perturb the basic solution by introducing a disturbance at a location x_0 on the interface:

$$H(T=0)=H_0(T=0)+H_D, \tag{2.13}$$

$$H_D=\varepsilon\exp[-W(\varepsilon X)^2]\cos(kX), \quad H_D=\varepsilon\exp[-W(\varepsilon X)^2]\cos(\omega T), \tag{2.14a,b}$$

where H_D denotes the imposed disturbance which can be either instantaneous or periodic, ε corresponds to the magnitude of the disturbance, W defines its range in the streamwise direction, and k and ω the wavenumber and frequency of the disturbance. The variable k is set to zero in simulations for the Froude number far from the critical regime, signifying an impulsive disturbance.

3. Stability analysis

3.1. *Linear stability analysis*

Linear stability analysis of the flow system under consideration has been performed by Timoshin (1997) and Pelekasis & Tsamopoulos (2001), assuming a constant film-flow rate and a constant rainfall rate, respectively, for the base flow. They introduced, on the base flow, small perturbations of the form

$$\left.\begin{aligned} &H = H_0 + \varepsilon f_{1,1} E, \quad U = U_0 + \varepsilon U_{1,1}(\overline{Y}) E, \quad P = \varepsilon P_{1,1} E, \\ &\Psi = \frac{\partial U_0}{\partial \overline{Y}} \frac{\overline{Y}^2}{2} + \varepsilon \Psi_{1,1}(\overline{Y}) E, \quad A = \varepsilon A_{1,1} E, \end{aligned}\right\} \tag{3.1}$$

where $\varepsilon \ll 1$ is a measure of the amplitude of the disturbance and $E = \exp(\mathrm{i}(kX - \omega_r T))$ represents the wavetrain, with k and ω_r being the complex wavenumber and complex frequency, respectively, which comprises the imposed disturbance. The eigenfrequency of the air–film system is numerically obtained as a function of the wavenumber and the problem parameters. Starting from asymptotic solutions in the limit of small gas-to-film-viscosity ratio, the dominant T–S and interfacial waves are captured via a continuation procedure in the parameter space for the two fluid systems of interest. This process is repeated in the present study for the problem formulation shown in § 2, which focuses on interfacial waves. In this fashion, both the air–water system and the air–de-/anti-icing fluid system were shown to be unstable with respect to interfacial disturbances. The rest of the parameters being held constant, the Froude number of these fluid systems is such that they are both well within the superctitical region, i.e. $Fr > Fr_{Cr}$; Fr_{Cr} is defined as the value of Fr for which $\omega_i = 0$, with $\partial \omega_i / \partial k_r > 0$.

In the special case where $\mathfrak{M} \to 0$, film inertia is insignificant, the case of air–de-/anti-icing fluid system, and upon demanding that shear rates evaluated on the gas and liquid sides of the interface balance each other, an asymptotic result is obtained for the stability of interfacial waves. In this fashion, Timoshin (1997) and Pelekasis & Tsamopoulos (2001) have obtained the following dispersion relation for interfacial waves:

$$\begin{aligned} \omega = {} & k H_0 \left.\frac{\partial U_0}{\partial Y'}\right|_{Y'=0} - \frac{\mathrm{i} H_0^3 k^4}{3We} - \mathrm{i}\frac{k^2}{Fr}\frac{H_0^3}{3} + \frac{H_0^2}{2}\left(-\left.\frac{\partial U_0}{\partial Y'}\right|_{Y'=0}\right) \\ & \times \frac{Ai(z=0)\left(\mathrm{i}k \left.\dfrac{\partial U_0}{\partial Y'}\right|_{Y'=0}\right)^{2/3} k|k| - \dfrac{2}{3}\left(\mathrm{i}k \left.\dfrac{\partial U_0}{\partial Y'}\right|_{Y'=0}\right) H_0 k|k| \, Ai'(z=0)}{|k|\left(\mathrm{i}k \left.\dfrac{\partial U_0}{\partial Y'}\right|_{Y'=0}\right)^{1/3} \displaystyle\int_\infty^0 Ai \, \mathrm{d}z + Ai'(z=0)\left(\left.\dfrac{\partial U_0}{\partial Y'}\right|_{Y'=0}\right)^2}, \end{aligned} \tag{3.2}$$

where Ai and Ai' denote the airy function and its first derivative, respectively, and $z = (ky)^{1/3}$; $Y' = y'/LRe^{-1/2}$. It can be easily shown that the numerical and asymptotic results agree very well when $\mathfrak{M}$ becomes vanishingly small; otherwise numerical solution is necessary.

Pelekasis & Tsamopoulos (2001), in their investigation of the above fluid systems, also identified the convective versus absolute nature of interfacial and T–S instabilities,

based on the properties of the dispersion relation in the complex plane (k, ω). It can be shown (Huerre & Monkewitz 1990) that upon application of a narrow pulse-like disturbance, the long-time system response is dominated by a wavepacket that is decaying along every ray X/T when it is stable or growing within a certain range of rays X/T when it is unstable. In the latter situation the system is considered as convectively or absolutely unstable depending on whether the ray $X/T = 0$ lies outside or inside the unstable wavepacket, respectively. Within the unstable wavepacket, unstable waves are dispersed and a certain complex wavenumber $k_* = k_{*r} + \mathrm{i}k_{*i}$ is dominant along specific spatiotemporal directions. The real group velocity, as is calculated based on k_*, is equal to the velocity along the specific ray:

$$\frac{\partial \omega_r}{\partial k_r}(k_*) = \frac{X}{T} = C_G, \tag{3.3}$$

while the growth rate along this ray is equal to $\sigma = \omega_i(k_*) - (X/T)k_{*i}$. The maximum growth rate within the wavepacket is recovered for the case with $k_{*,i} = 0$ (temporal analysis). The wavenumber k_{max} for which $\partial \omega_i / \partial k|_{k=k_{max}} = 0$ provides the wavelength of the wave with maximum growth rate, $\omega_{i,max} = \omega_i(k_{max})$. Clearly, when $\omega_{i,max} > 0$ the flow is linearly unstable, while if $\omega_{i,max} < 0$ the flow is characterized as linearly stable. In this fashion Pelekasis & Tsamopoulos (2001) were able to identify the T–S waves as convectively unstable and the interfacial waves as convectively or absolutely unstable depending on the Froude number. In particular, as the Froude number increases the nature of instability of interfacial waves was seen to shift from convective to absolute.

Evaluation of the group velocity of the different waves comprising the unstable wavepacket can be performed by two different approaches (Brevdo *et al.* 1999). The pinching method (Huerre & Monkewitz 1990; Brevdo *et al.* 1999), also known as the collision method, can be used along any ray X/T in order to determine the wavenumber k and the transformed frequency $\omega_V = \omega - kV_G$ for which $\mathrm{d}\omega_V/\mathrm{d}k = 0$. The transformed dispersion relation $D_V(\omega_V, k; V_G) = 0$ is used and the two branches $k_\pm = k_\pm(\omega_V; V_G)$ are calculated as a function of ω_{Vr} until, for some ω_{Vi}, the two branches collide at a certain value of k_0; the $\pm$ sign denotes branches stemming from the positive/negative semi-plane of the k complex plane. Then, $\omega_0 = \omega_{V0} + k_0 V_G$ and k_0 denote the frequency and wavelength of the specific ray X/T whose group velocity is

$$V_{GR} = \frac{X}{T} = \frac{\partial \omega_r}{\partial k_r} \quad \text{with} \quad \left.\frac{\partial \omega_i}{\partial k_r}\right|_{k=k_r+\mathrm{i}k_i} = 0. \tag{3.4}$$

Starting from the wavepacket with maximum amplification the calculation proceeds until two limiting group velocities are obtained, namely the one corresponding to the right edge of the wavepacket, V_{GR}, pertaining to the fastest moving waves, and the one corresponding to the left edge, V_{GL}, pertaining to the slowest among the unstable waves.

Alternatively, the characteristics along the rays that include the unstable wavepacket can be estimated with the saddle-point technique (Brevdo *et al.* 1999). Specifying the imaginary part of the wavenumber to be different from zero, $k_{0i} \neq 0$, the wavenumber, frequency and group velocity of the waves comprising the unstable wavepacket are obtained as $\omega_0 = \omega(k = k_{0r} + \mathrm{i}k_{0i})$, with $\partial \omega_i / \partial k_r|_{k=k_{0r}+\mathrm{i}k_{0i}} = 0$, $V_G = X/T = \partial \omega_r / \partial k_r|_{k=k_{0r}+\mathrm{i}k_{0i}}$. Again $\sigma_i = \omega_i - V_{GR} k_i \approx 0$ provide the left and right edges of the unstable wavepacket. Even though the collision method is much more time-consuming than the saddle-point method in many studies, the latter fails to deliver reliable results, as was the case with the stability analysis of flow down

an inclined plane (Brevdo *et al.* 1999). Similar technical difficulties were encountered upon application of the saddle-point technique in the present study as well. Therefore, all the results presented henceforth have been obtained with the pinching method.

3.2. *Weakly nonlinear stability analysis*

Linear stability analysis is unable to describe the evolution of even small disturbances over long time intervals, within which nonlinear effects become important. In this time scale, instabilities tend to become saturated provided that the parameter range remains close to criticality in conjunction with the sub-/supercritical nature of the bifurcating solution. In this fashion, fluid systems like the one examined here can be investigated for steady travelling waveforms. The proper framework for studying interfacial wave phenomena is provided by the multiple-time-scale method (Benjamin 1961; Stewartson & Stuart 1971; Lin 1974; Bender & Orszag 1978) that leads to the nonlinear Schrödinger equation describing the amplitude modulation of the emerging wave. In its more general form, the one accounting for long-time growth of the unstable mode, the latter equation assumes the form of the nonlinear complex Ginzburg–Landau equation (Saarlos & Hohenberg 1992). It also contains the nonlinear contribution to growth and saturation of the unstable wave, as a result of mode interaction.

In this section the weakly nonlinear behaviour of a linearly unstable wave is examined in the limit $\mathfrak{M} \to 0$. Using appropriate scales in time and space we investigate the effect of nonlinear interaction on the evolution of the emerging wave. It was shown by Benjamin (1961) for two-dimensional linear dispersive waves down an inclined plate and Stewartson & Stuart (1971) for plane Poiseuille flow that unstable wavepackets are dispersed in a time of order ω_i^{-1} and occupy a characteristic length of order $\omega_i^{-1/2}$, where ω_i denotes the maximum growth rate among the unstable waves. Such a behaviour is valid for a wide range of wave phenomena, including the case of capillary waves on films examined here. If we concentrate on waves for which the maximum growth rate is very close to the linear neutral curve, $\omega_i \to 0$, the characteristic time of order ω_i^{-1} is quite large and consequently nonlinear effects should be accounted for. Similarly, near the edges of the unstable wavepacket for the case of de-/anti-icing fluids whose parameter range is far from criticality, the amplitudes remain small and the nonlinear modulation of the carrier wave can be characterized as weak. Thus, we introduce on the interface a small localized disturbance of the form

$$H_D = \varepsilon[D(\varepsilon X)\mathrm{e}^{\mathrm{i}kx} + D^*(\varepsilon X)\mathrm{e}^{-\mathrm{i}kX}], \quad D(\varepsilon X) = d(\varepsilon X; \tau = 0), \quad d \equiv f_{1,1}, \tag{3.5}$$

which is characterized by a small amplitude ε; the asterisk in superscript denotes complex conjugation. Equation (2.14*a*) provides an example of an acceptable form of disturbance function $D(\varepsilon X)$. When $\omega_i = O(\varepsilon^2)$ the effect of nonlinearity can be observed over a period of time of order $O(\varepsilon^{-2})$ and for a distance of order $O(\varepsilon)$. In order to properly account for these effects the following scalings are introduced:

$$\xi = X - C_p T, \quad \zeta = \varepsilon(X - C_G T), \quad \tau = \varepsilon^2 T, \quad \zeta_1 = \varepsilon^2(X - C_G T), \tag{3.6}$$

where C_p and C_G denote the phase and group velocities, respectively, of the wave E as predicted from linear theory. In this fashion the amplitude modulation, $f_{1,1} \equiv d$, of the wave $E = \exp(\mathrm{i}(kX - \omega_r T))$ can be obtained near critical conditions, $\omega = \omega(k; Fr, We, H_0, \lambda) = \omega_r + \mathrm{i}\omega_i$, with $\omega_i = O(\varepsilon)$, as it varies over the slow time and space coordinates τ and ζ. The evolution equation is obtained as a solvability condition for the $O(\varepsilon^3)$ problem and is known as the complex nonlinear Ginzburg–Landau equation. This is the order to which nonlinear mode interaction produces the

carrier wave E. Mode interactions producing E° Fourier modes are also accounted for. Since there is no mean-flow perturbation to $O(\varepsilon)$, mean-flow or long-wave components are first obtained to $O(\varepsilon^2)$ due to self-interaction of the primary wave E with its complex conjugate $E^* = \exp(-\mathrm{i}(kX - \omega_r T))$. A short outline of the derivation as well as implications of the above described interactions to the system dynamics are presented and discussed in the following.

The stream function in the gas phase and the shape of the interface are expressed as follows:

$$\Psi = \lambda \frac{\overline{Y}^2}{2} + \Phi, \quad H = H_0 + f, \tag{3.7a,b}$$

where $\lambda \overline{Y}^2/2$ and H_0 are the base-flow results for the stream function and the location of the interface. Consequently, the x-momentum reads as

$$\frac{\partial^4 \Phi}{\partial \overline{Y}^4} = \left(\lambda \overline{Y} + \frac{\partial \Phi}{\partial \overline{Y}}\right) \frac{\partial^3 \Phi}{\partial X \partial \overline{Y}^2} - \frac{\partial \Phi}{\partial X} \frac{\partial^3 \Phi}{\partial \overline{Y}^3}, \tag{3.8}$$

while the boundary conditions outside the viscous sublayer give

$$\frac{\partial \Phi}{\partial \overline{Y}}(\overline{Y} \to \infty) = \lambda(A + f), \tag{3.9}$$

$$\frac{\partial^2 \Phi}{\partial \overline{Y}^2}(\overline{Y} \to \infty) = 0. \tag{3.10}$$

Finally, the governing equation in the film assumes the form

$$\begin{aligned} \frac{\partial f}{\partial T} = &-\frac{\partial}{\partial X}\left(\frac{(H_0+f)^2}{2}\left(\lambda + \frac{\partial^2 \Phi}{\partial \overline{Y}^2}\right)\right) + \frac{\partial}{\partial X}\left(\frac{(H_0+f)^3}{3}\frac{\partial P}{\partial X}\right) \\ &- \frac{\partial}{\partial X}\left(\frac{(H_0+f)^3}{3We}\frac{\partial^3 f}{\partial X^3}\right) + \frac{\partial}{\partial X}\left(\frac{(H_0+f)^3}{3}\frac{(\rho_w/\rho - 1)}{Fr}\frac{\partial f}{\partial X}\right), \end{aligned} \tag{3.11}$$

whereas on the gas–liquid interface we obtain

$$\overline{Y} = 0: \quad \Phi = \frac{\partial \Phi}{\partial \overline{Y}} = 0. \tag{3.12}$$

Following the derivation of Djordjevic & Redekopp (1977) for two-dimensional wavepackets of capillary–gravity waves, functions Φ and f as well as the pressure and displacement thickness can be expanded as follows:

$$\Phi = \varepsilon \Phi_1(\xi, \zeta, \zeta_1, \overline{Y}, \tau) + \varepsilon^2 \Phi_2(\xi, \zeta, \zeta_1, \overline{Y}, \tau) + \varepsilon^3 \Phi_3(\xi, \zeta, \zeta_1, \overline{Y}, \tau) + O(\varepsilon^4), \tag{3.13}$$

$$f = \varepsilon f_1(\xi, \zeta, \zeta_1, \tau) + \varepsilon^2 f_2(\xi, \zeta, \zeta_1, \tau) + \varepsilon^3 f_3(\xi, \zeta, \zeta_1, \tau) + O(\varepsilon^4), \tag{3.14}$$

$$P = \varepsilon P_1(\xi, \zeta, \zeta_1, \tau) + \varepsilon^2 P_2(\xi, \zeta, \zeta_1, \tau) + \varepsilon^3 P_3(\xi, \zeta, \zeta_1, \tau) + O(\varepsilon^4), \tag{3.15}$$

$$A = \varepsilon A_1(\xi, \zeta, \zeta_1, \tau) + \varepsilon^2 A_2(\xi, \zeta, \zeta_1, \tau) + \varepsilon^3 A_3(\xi, \zeta, \zeta_1, \tau) + O(\varepsilon^4). \tag{3.16}$$

Substituting the above expressions in the governing equations we obtain a series of problems in ascending powers of ε. To leading order the linear-stability-analysis formulation and the corresponding solution are recovered (see (A 1)–(A 9) in the Appendix), involving only the fundamental harmonic, $E = \exp(\mathrm{i}k(X - c_p T)) = \mathrm{e}^{\mathrm{i}k\xi}$, and its complex conjugate E^{-1}:

$$\left.\begin{aligned} &\Phi_1 = \Phi_{1,1}(\zeta, \tau, \overline{Y})E + \text{c.c.}, \quad f_1 = f_{1,1}(\zeta, \tau)E + \text{c.c.}, \\ &A_1 = A_{11}(\zeta, \tau)E + \text{c.c.}, \quad P_1 = P_{11}(\zeta, \tau)E + \text{c.c.} \end{aligned}\right\} \tag{3.17}$$

Coefficients Φ_{11}, A_{11} and P_1 are obtained as linear functions of $f_{11} = d$ while substitution in (A 6), which is the linearized form of (2.12), recovers the dispersion relation, i.e. (3.2).

To second order we are looking for a solution of the $O(\varepsilon^2)$ problem (see (A 10)–(A 15)), which is of the form

$$\Phi_2 = \Phi_{2,0}(\xi, \zeta, \zeta_1, \overline{Y}, \tau)E^0 + \Phi_{2,1}(\xi, \zeta, \zeta_1, \overline{Y}, \tau)E + \Phi_{2,2}(\xi, \zeta, \zeta_1, \overline{Y}, \tau)E^2 + \text{c.c.}, \quad (3.18)$$

$$f_2 = f_{2,0}(\xi, \zeta, \zeta_1, \tau)E^0 + f_{2,1}(\xi, \zeta, \zeta_1, \tau)E + f_{2,2}(\xi, \zeta, \zeta_1, \tau)E^2 + \text{c.c.}, \quad (3.19)$$

with the pressure, P_2, and displacement thickness, A_2, assuming similar expressions with the position of the interface, f_2. Clearly, the second-harmonic and mean-flow components arise due to interaction of the fundamental harmonic with itself and its complex conjugate, respectively.

Upon integration of the mean-flow component (see (A 16)–(A 18)) of the $O(\varepsilon^2)$ problem and application of the boundary conditions it can be shown that

$$\frac{\partial^2 \Phi_{2,0}}{\partial \overline{Y}^2} = \mathrm{i}k \int_{\infty}^{\overline{Y}} \left(\Phi_{1,-1} \frac{\partial^2 \Phi_{1,1}}{\partial \overline{Y}^2} - \Phi_{1,1} \frac{\partial^2 \Phi_{1,-1}}{\partial \overline{Y}^2} \right) \mathrm{d}s. \quad (3.20)$$

Thus, the mean-flow component of the solution is a result of the Reynolds stress that manifests itself in the interaction between the fundamental component and its conjugate. The effect of viscous Reynolds stresses near the interface was shown by Craik (1966) to be essential for growth of interfacial waves in water–air systems and was also shown to play a central role in another type of wave propagation, namely that of the critical neutral mode in plane Poiseuille flow between parallel plates (Davey, Hocking & Stewartson 1974). In the present problem it is essential for generating the mean-flow component that exchanges energy with the unstable wavepacket until it eventually dominates the flow. The mean-flow component of the interface is indeterminate to this order and will be part of the solvability condition to $O(\varepsilon^3)$. The fundamental component of the second-order solution consists of a homogeneous part that is similar to the one obtained for the $O(\varepsilon)$ case (see (A 7)–(A 9)) and a particular solution that is analogous to $\partial d/\partial \zeta$. Upon substitution in the $O(\varepsilon^2)$ equation for the interface (see (A 22)), a condition for the fundamental component of the interfacial position is obtained. Terms stemming from the homogeneous solution reproduce the dispersion relation (3.2) and consequently vanish, whereas terms containing the slow spatial derivative, $\partial d/\partial \zeta$, of the modulation d of the interfacial position provide the group velocity of the propagating wave.

To $O(\varepsilon^3)$ nonlinear mode interaction, $|d|^2 d$, enters the dynamics of the fundamental harmonic E (see (A 27)–(A 31)), as can be gleaned from the solution for the fundamental component of the interface shown in (A 31). Substituting in (A 30), representing the fundamental component of (2.12) to $O(\varepsilon^3)$, we obtain a solvability condition for the amplitude modulation of the interface $d(\tau, \zeta)$. It should be stressed that linear terms involving coefficient e from the solution of the fundamental component of the interface provided in (A 31) cancel out in this process since they reproduce dispersion relation (3.2), whereas linear terms arising from (A 30) and involving derivatives $\partial d/\partial \zeta_1$ and $\partial \alpha/\partial \zeta$ also cancel out as they reproduce the relationship for the group velocity. The remaining terms in (A 30) satisfy a partial differential equation (PDE) of the form

$$\frac{\partial d}{\partial \tau} + S_1 \frac{\partial^2 d}{\partial \zeta^2} = S_2 d + S_3 d\,|d|^2 + S_4 f_{20} d \quad (3.21)$$

for the amplitude modulation d of the fundamental wave E. $S_2 = \pm\omega_i'/k_r$ is positive or negative when Fr is larger or smaller, respectively, than a critical value of $Fr = Fr_{Cr}$ for which $\omega_i = \omega_i' = 0$. In the present study ω_i' is set to $\pm \mathrm{d}\omega_i/\mathrm{d}Fr|_{Fr \to Fr_{Cr}}$ in order to signify regions above and below criticality, so that $\varepsilon^2\omega_i' \sim O(1)$.

In the absence of fundamental and mean flow interaction, (3.21) assumes the well-known form of Schrödinger's equation that is used in order to describe the nonlinear behaviour of interfacial waves for parameters close to the linear neutral curve or near the outskirts of a wavepacket where growth rate is also very small. It also answers important questions regarding the existence of travelling waves and fronts in its area of validity (Saarlos & Hohenberg 1992).

When interaction between the fundamental wave and the mean flow is present (3.21) alone is not enough to describe the dynamics since evaluation of $f_{2,0}$ is also required. The latter is obtained via (A 32) which, given the expressions for $f_{1,1}$, $f_{1,-1}$ and $\Phi_{2,0}$, assumes the form

$$(H_0\lambda - c_G)\frac{\partial f_{2,0}}{\partial \tau} = S_5 \frac{\partial |d|^2}{\partial \zeta}. \tag{3.22}$$

Equations (3.21) and (3.22) can be solved simultaneously in order to provide the evolution of the amplitude modulation $f_{1,1} = d$ of the fundamental harmonic along with the mean-flow component $f_{2,0}$. Clearly then, when the group velocity C_G of the fundamental wave E happens to coincide with the product between the dimensionless film thickness and shear stress exerted by the gas stream on the film in the base-flow configuration, $H_0\lambda$, there is resonance between the two Fourier components and consequently energy transfers towards long-wave formation. Upon inspection of dispersion relation (3.2) of interfacial waves when $\mathfrak{M}$ tends to zero, it can be shown that the phase speed of long waves, recovered as k tends to zero, is $C_p = \omega/k = H_0\ \partial U/\partial Y'(Y' = 0) = H_0\lambda$.

A similar result was obtained by Djordjevic & Redekopp (1977) for two-dimensional capillary–gravity Stokes waves. They also arrived at a Davey–Stewartson-type set of equations like (3.21) and (3.22) and stressed that the limit of small liquid depth is more appropriate for resonance between the advancing wavepacket and the emerging long waves. In the present study, as well as in the case of Stokes waves, growth of the mean-flow component, eventually leading to long-wave formation, is initiated by the self-interaction of the short waves, i.e. a Reynolds-stress type of interaction arising to $O(\varepsilon^2)$. When resonance takes place the scaling used in the above analysis is not relevant any more and rescaling is necessary to capture the system dynamics. Djordjevic & Redekopp proceeded in this direction in order to eliminate the secular terms. The rescaled set of equations was directly integrated in terms of elliptic functions (Ma & Redekopp 1979), and the solution assumes the form of a solitary wave with a phase jump:

$$d = K(C)^{1/2}\exp\left[\mathrm{i}\frac{C}{2}\left(x - \frac{C}{2}T\right)\right]\tanh[K(x - CT)], \quad \Phi_{0,\zeta'} = -2K^2\sec h^2[K(x - CT)]. \tag{3.23}$$

In the same study it was shown that the rescaled equations admit a uniform-wavetrain solution which is always unstable to modulational sideband instabilities. A connection between the uniform wavetrain and the solitary-wave solutions was conjectured by Ma & Redekopp but was not verified. Simulations performed in the context of the present study reveal that the emerging interfacial waves tend to

form a uniform wavetrain that, however, never saturates fully. Rather, it becomes unstable and eventually produces a phase-jump-type solitary-wave solution. Rescaling in the manner of Djordjevic & Redekopp is not attempted herein, as we are mostly interested in revealing the mechanism behind long-wave and soliton formation in our simulations, and the fluid systems of interest, i.e. de-/anti-icing fluids or water with air, are far from criticality in which case the above analysis is strictly valid only near the edges of the unstable wavepacket. It is known (Craik 1985) that modulation of long waves about $k=\omega=0$ leads to soliton formation via the Korteweq–de Vries equation. In a recent study it was shown by Clamond & Germain (1999) that the proper interaction between a Stokes wavepacket and a long wave, one that is able to capture the shape modulation of the latter, is via a coupled cubic Schrödinger and Korteweq–de Vries set of equations. In other words, it entails interaction between a Stokes wavepacket and a solitary wave. The latter issue was first addressed by Ma & Redekopp (1979) by obtaining the next order correction to (3.41) and pointing out the connection with Korteweq–de Vries theory for long waves and the nonlinear Schrödinger theory for short waves. As was pointed out in §1, a similar soliton–wavepacket interaction was identified as the dominant mechanism behind spike formation in the evolution of high-frequency T–S waves (Kachanov *et al.* 1993; Li *et al.* 1998). Consequently, when short- to long-wave resonance is present, in the manner relevant to the Stokes waves and interfacial waves arising in the present study, it can be argued based on the above that solitary-wave formation will eventually prevail. In the following it will be shown, by careful interpretation of the results of numerical simulations, that short- to long-wave resonance, in the manner described above, and soliton formation can explain the wave patterns obtained in the numerical results presented in I.

4. Dynamic simulations and interpretation of results

In this section we present results of numerical simulations for the case of interfacial wave growth, including film inertia when necessary. The study focuses on the cases of a water film or a film of de-/anti-icing fluid being dragged by a boundary layer of air, which sets the viscosity ratio μ/μ_w to relatively low values and validates the assumption of quasi-steady state in the gas phase. A detailed outline of the numerical methodology is provided in I. Properties for the de-/anti-icing fluid–air system are obtained from Ozgen *et al.* (2002), $\mu/\mu_w = 1.67\times10^{-6}$ and $\rho/\rho_w = 0.001$, while a flow arrangement characterized by a test section of length $L\approx30\,\mathrm{cm}$ and a free stream velocity, U_∞, ranging between 10 and $40\,\mathrm{m\,s^{-1}}$ is envisioned as it covers a wide range of available experimental investigations. For the air–water system μ/μ_w and ρ/ρ_w are set to 0.018 and 0.001, respectively. In this context, when $L\approx30\,\mathrm{cm}$ and $U_\infty\approx30\,\mathrm{m\,s^{-1}}$, $Fr = 92699, 3.94\times10^4$ and $We = 46, 59.88$ for the cases of water and deicing fluid, respectively. The film thickness necessary for the triple-deck approach to be valid is $H_f\sim LRe^{-5/8}\approx0.06\,\mathrm{mm}$, i.e. $Re\sim8\times10^5$, which is of the order of film measurements on airfoils under simulated rainfall conditions; a moderate rainfall rate of the order of $100\,\mathrm{mm\,h^{-1}}$ was assumed in obtaining the above estimates (Smyrnaios *et al.* 2000; Pelekasis & Tsamopoulos 2001). The mesh characteristics in the bulk of the simulations are $\Delta X=0.2$, $\Delta\overline{Y}=0.4$, $\Delta T=0.001$ and $\overline{Y}_\infty=10$. Simulations with $\Delta X=0.1$ and $\Delta\overline{Y}=0.2$ were conducted not only to capture the effects related to film inertia, which leads to smaller wavelengths and more intense recirculation patterns, but also to validate the results via mesh refinement. Both cases near the critical neutral curve as well as away from it are explored and an attempt is made to interpret

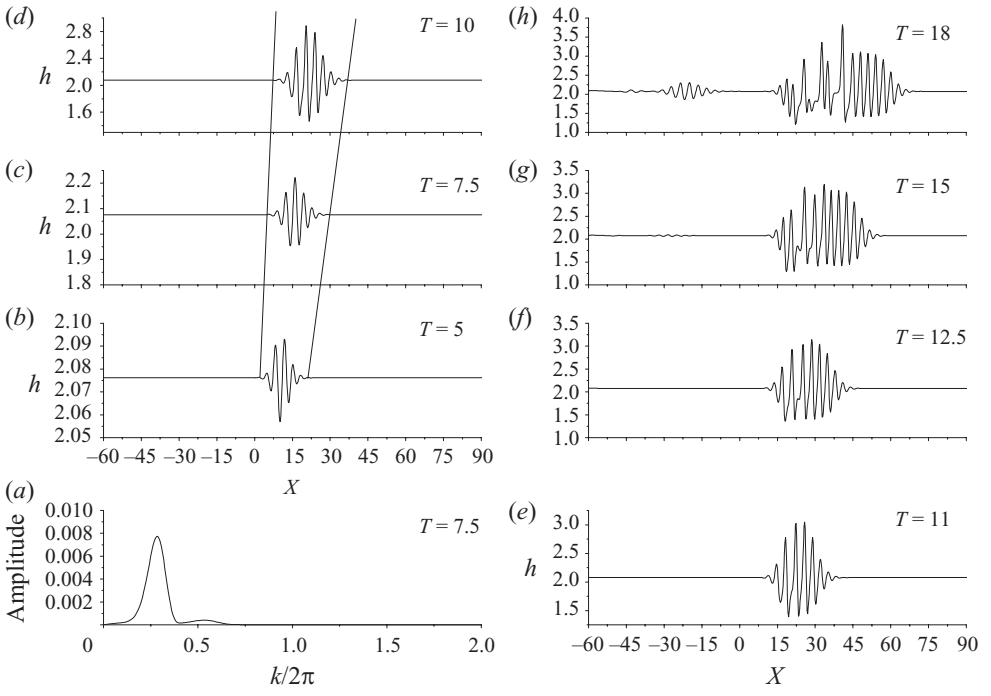

FIGURE 1. (*a*) Fourier transform and (*b–h*) snap-shots of interfacial waves for the air–deicing system in response to an impulsive disturbance; $H_0 = 2.07$, $\varepsilon = 0.001$, $x_0 = 0.8$, $We = 60$ and $\bar{Fr} = 3.94 \times 10^4$.

the results in terms of spike formation and the resonance mechanism presented in § 3.

4.1. *Evolution of interfacial waves in the limit of negligible film inertia, $M \ll 1$*

First, the possibility for formation of steady travelling waves is investigated. Previous studies have either conjectured the existence of steady travelling waveforms in the context of the condensed layer limit and for a thin film flow over external aerodynamic surfaces (Rothmayer, Matheis & Timoshin 2002), or established a supercritical bifurcation via weakly nonlinear analysis (Blennerhassett 1980) for interfacial waves in a stratified channel flow. However, in the latter case, numerical evaluation of the coefficients of the Schrödinger equation was ambiguous at large Reynolds numbers. As will be seen in detail in the following, simulations conducted in the present study did not indicate formation of steady waveforms with characteristics in the vicinity of predictions by linear theory. Figure 1 illustrates the evolution of the interface of a deicing fluid over a time interval that covers linear growth and nonlinear effects. Table 1 contains the predictions of linear theory and the results of Fourier transform on the spatiotemporal evolution of the wavepacket, for the frequency, wavelength and group velocity of the most amplified wave of the wavepacket. There is a tendency for front formation and propagation of a saturated wave with characteristics that are close to the attributes of the propagating linear wavepacket. Figure 1(*a*) illustrates the Fourier spectrum at a relatively early time when the wavelength predicted by linear theory is dominant. However, as clearly illustrated in figure 1(*g*, *h*), this is not materialized because it is eventually superseded by the onset of long waves and spike formation and this behaviour is recovered for almost the entire parameter

	Linear theory ($Fr = 3.94 \times 10^4$)	Numerical results ($Fr = 3.94 \times 10^4$)	Linear theory ($Fr = Fr_{Cr} = 3.94 \times 10^3$)	Linear theory ($Fr = 1.82 \times 10^4$)
Wavelength	3.47	3.53	15	3.6
Period	2.32	2.34	14	2.45
C_G	2.2	2.26	1.4	2.05
C_{GL}	0.4	0.4		0.73
C_{GR}	2.75	2.7		3.7

TABLE 1. Attributes of the unstable wavepacket for interfacial waves of the air–deicing system predicted analytically via (3.2) and computed numerically; $x_0 = 0.8$, $\lambda = 0.37$, $H_0 = 2.076$, $We = 60$ and $H_0\lambda \approx 0.77$. C_G: group velocity of the most unstable wave of the wavepacket; C_{GL}: group velocity of the left wave of the unstable wavepacket; C_{GR}: group velocity of the right wave of the unstable wavepacket.

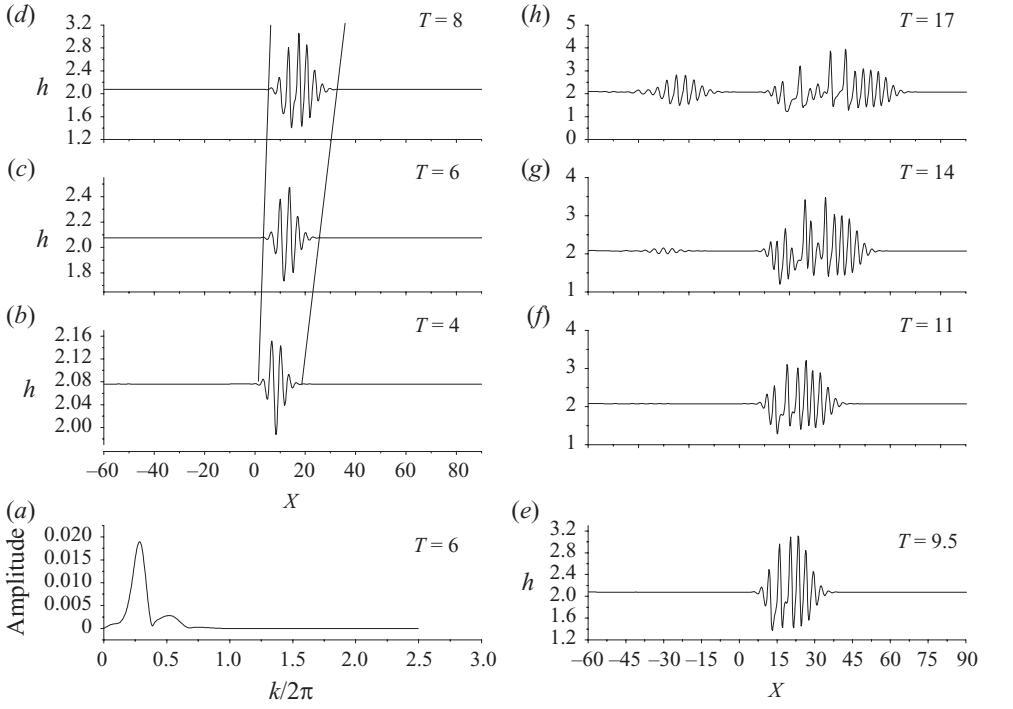

FIGURE 2. (*a*) Fourier transform and (*b–h*) snap-shots of interfacial waves for the air–deicing system in response to an impulsive disturbance; $H_0 = 2.07$, $\varepsilon = 0.01$, $x_0 = 0.8$, $We = 60$ and $Fr = 3.94 \times 10^4$.

range examined herein. Repeating the simulation with a larger amplitude of the initial disturbance simply accelerates the onset of spike formation (figure 2), without modifying the soliton-type wave pattern with maximum height that is, roughly, twice the mean film thickness H_0. Consequently, and in order to fully illustrate the different dynamic phenomena associated with the evolution of interfacial waves, we use relatively small values of the amplitude, $\varepsilon \leqslant 0.5$, of the initial disturbance in the simulations to be presented in the following. It should be stressed that, as illustrated in figures 1 and 2 as well as in all the simulations to be presented, long waves appear from the left side of the advancing wavepacket since it is there that the resonance criterion, $H_0\lambda = C_G$, is met.

Upon inspection of figures 1 and 2 one notices the onset and growth of an additional wavepacket from the left side of the computational domain (figures 1g,h and 2g,h). The latter is numerically generated, and it possesses all the characteristics of the most unstable wavepacket predicted by linear theory and arises because of truncating the infinite domain in the longitudinal direction. As was discussed in I it amounts to an infinitesimal disturbance imposed on the left edge of the computational domain, the level of which is determined by the accuracy of double-precision arithmetic. It, however, does not affect the evolution of the leading wavepacket as long as their distance remains large. Interaction between the wavepacket advancing from the left edge of the domain and the main disturbance may arise when, for large amplitudes of the initial disturbance, waves travelling to the left of x_0 reach the advancing wavepacket before they decay significantly. Then different waveforms may arise due to wave collision in the wake of the leading wavepacket, which, again, do not influence its dynamics as long as they remain far enough, as is the case with figures 1 and 2. This effect may also explain small differences in the evolution of the second wavepacket, as is manifested in figures 1(g,h) and 2(g,h). It should also be stressed that, as was pointed by Timoshin & Smith (2003), non-local interactions of the type described above may lead to feedback instability and the appearance of global structures depending on the attributes of the interacting waves. However, such an extreme dynamic distortion of the flow arrangement was not observed in the present study.

It is known from linear theory (Pelekasis & Tsamopoulos 2001) that Fr controls the onset of instability for interfacial waves. Since, for the parameter range of de-/anti-icing films in air, interfacial waves are well away from criticality, i.e. $\omega_i > 0$, it will be useful to examine the behaviour of this system for $Fr = Fr_{Cr}$, with the rest of the parameters remaining the same as for the case of a deicing fluid, via weakly nonlinear analysis in which case the approach outlined in § 3 is strictly valid. Once the characteristics of travelling monochromatic waves near criticality are known then such waves can be incorporated in the simulations in the form of an initial disturbance to be followed numerically until saturation. This process can then be repeated until the actual Fr for the de-/anti-icing fluid–air system is reached.

Gradually varying Fr in this fashion, linear analysis provides $Fr_{Cr} \sim 3940$, with $\omega_{i,max} \sim 0.019$. Figure 3$(a$–$f)$ portrays the dispersion relation for this situation. Performing weakly nonlinear analysis around the linear wave $E = \exp(\mathrm{i}(kX - \omega T))$ at critical conditions gives $S_3 \approx 49.5 - 39\mathrm{i}$, which amounts to a subcritical bifurcation (Saarlos & Hohenberg 1992); $S_1 = 100.76 - 27.8\mathrm{i}$ while S_2 is obtained in the manner explained in the § 3.2. Consequently, if travelling waves are to be observed at all they should be expected in the subcritical region, i.e. Fr close to but smaller than Fr_{Cr} of the parameter space. By carrying out numerical simulations for Fr slightly below the critical value, we obtain interfacial waves exhibiting a wavepacket that propagates and possesses the characteristics predicted by linear theory, while its amplitude decreases slowly but steadily. On the other hand, above the critical Fr a wavepacket is not formed. Rather the disturbance tends to saturate near the peaks of the waves, whereas it develops regions of increasing curvature around the troughs. At the same time waves of progressively smaller wavelength appear that also gradually grow and occupy an increasingly large part of the interface. This is an indication of sideband instability and is also manifested in the Fourier spectrum that is distinctly broadband when extended to large wavenumbers. Beyond a certain point in time the simulations cannot proceed due to loss of accuracy around the troughs, indicating the tendency for cusp formation.

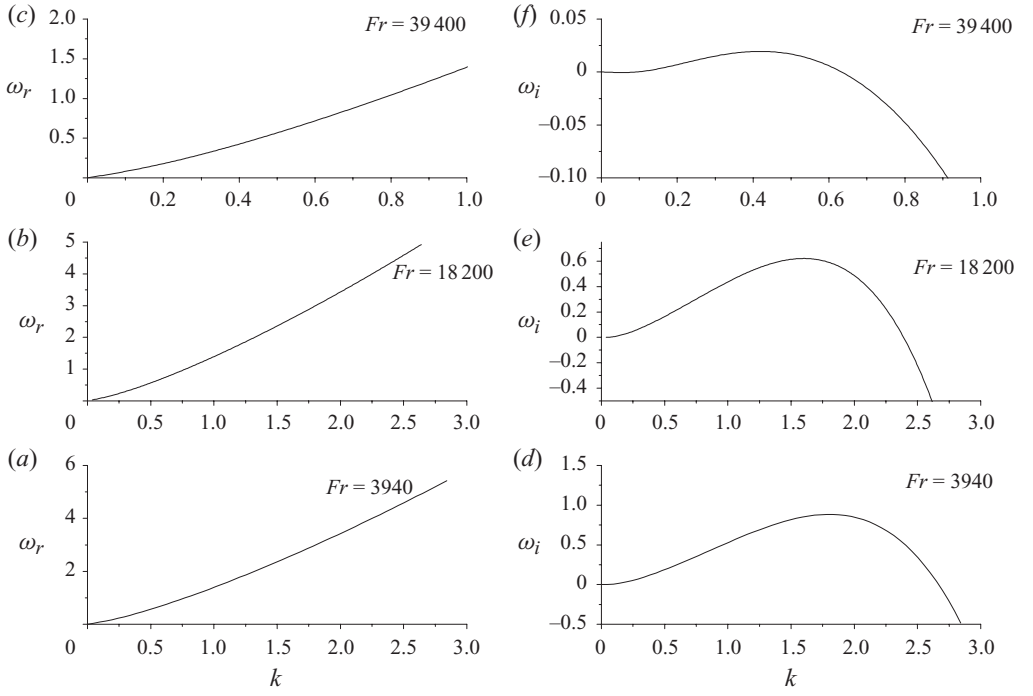

FIGURE 3. Dispersion relation, $\omega_r = \omega_r(k)$ and $\omega_i = \omega_i(k)$, corresponding to interfacial waves for the air–deicing system, when (*a*, *d*) $Fr = 3.94 \times 10^3$, (*b*, *e*) $Fr = 1.82 \times 10^4$ and (*c*, *f*) $Fr = 3.94 \times 10^4$.

Thus, the findings of weakly nonlinear analysis and the results of numerical simulations concur with the existence of a subcritical bifurcation at Fr_{Cr}. In fact, progressively larger values of amplitude ε were used with $Fr < Fr_{Cr}$, without ever producing a saturated wave. The propagating wavepacket that appeared as a result of the initial disturbance always tended to die out eventually. It seems that the level of shape perturbation that is required for subcritical destabilization to take place, i.e. for a steady travelling wave to appear in the parameter range for which the base flow is stable, is very large. Similarly, further increasing Fr provided a system response exhibiting very large curvature around the troughs of the wave. The details of the singularity that is about to form in this region of the interface were not pursued herein. Given the fact that this range of Fr does not correspond to either of the two fluid systems that we investigated in this study we did not pursue this search further, relegating it to a future study.

As Fr is increased further there is a threshold value, roughly $Fr = 1.8 \times 10^4$, beyond which the response of the interface to an impulsive initial disturbance is of the type shown in figures 1 and 2. This is the minimum value of Fr for which the pattern of saturated spike formation is obtained. As illustrated by the dispersion relation relevant to this parameter range (figure 3*b*, *e*), there is a band of unstable wavenumbers, with $k = 3.6$ being the most unstable one. During the phase of linear growth the latter wavenumber dominates the spatial Fourier spectrum. Estimating the group velocities corresponding to the left ($C_{GL} = 0.73$) and right ($C_{GR} = 3.7$) travelling waves of the wavepacket as well as the group velocity ($C_G = 2.05$) of the most unstable wave (table 1), it is seen that the phase velocity of long interfacial

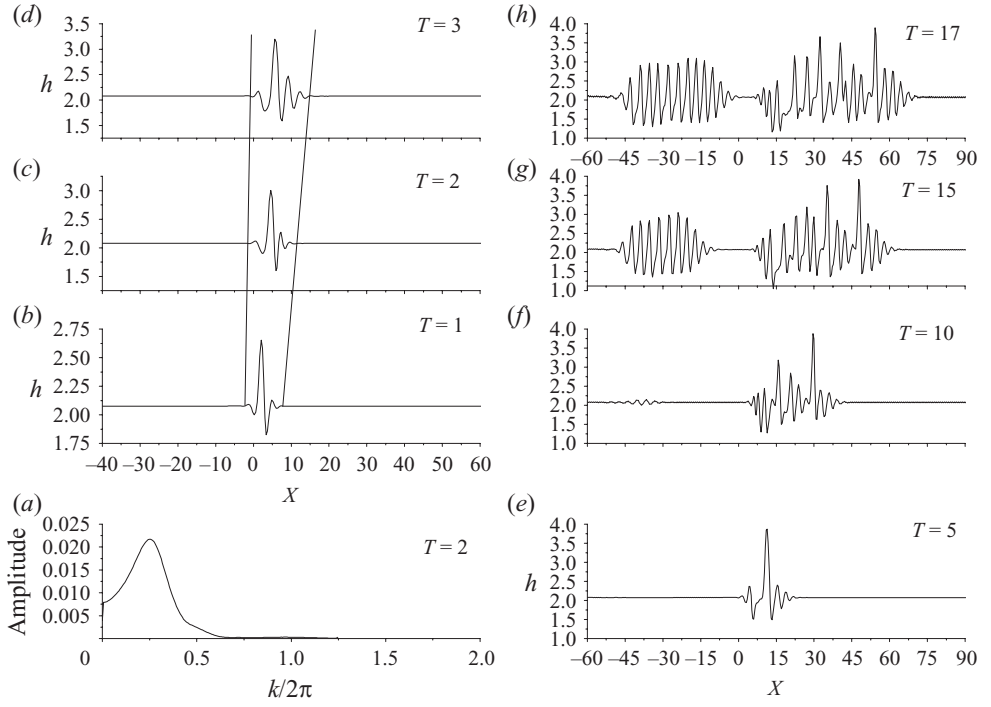

FIGURE 4. (*a*) Fourier transform and (*b–h*) snap-shots of interfacial waves for the air–deicing system in response to an impulsive disturbance; $H_0 = 2.07$, $\varepsilon = 0.4$, $x_0 = 0.8$, $We = 60$ and $Fr = 3.94 \times 10^4$.

waves, $C_p = H_0\lambda = 0.77$ based on the limit of (3.12) as k tends to zero, marginally falls inside the interval (C_{GL}, C_{GR}). Beyond the threshold value $Fr = 1.8 \times 10^4$, including the value of $Fr = 3.94 \times 10^4$ corresponding to the anti-icing fluid under examination, the response of the interface assumes the form of a travelling wavepacket that also spreads out from its centre of most intense growth (see also figures 1 and 2). Table 1 provides the relevant group velocities for this case, which clearly contain the phase speed of long waves $H_0\lambda$. Consequently, there is a possibility for short- to long-wave resonance and this is observed in the simulations. Indeed, the wavepacket almost saturates to form steady travelling waves especially for small amplitudes (figures 1 and 2); however, it loses stability to waves of much larger wavelength. In fact, as it turns out, $C_{GL} < H_0\lambda < C_G$, and the wavepacket always starts disintegrating on its left side, forming long waves that evolve and modulate until they reach a saturation height that is almost twice the mean film height H_0. In this process their speed keeps increasing while their shape downstream and upstream of the spike exhibits capillary waves and a depression region, respectively, in a manner typically observed in soliton formation. Behind the leading spike other spikes tend to form that eventually reach the same maximum height. This pattern persists for the entire range of amplitudes examined, $0.001 \leqslant \varepsilon \leqslant 0.5$; figures 4 and 5 correspond to $\varepsilon = 0.4$ and 0.5. In fact, when $\varepsilon = 0.4$ and 0.5 the dynamics evolve faster and a second peak is also captured with a similar capillary-wave formation ahead of it as for the leading peak (figures 4 and 5). Once the leading wave attains the state dominated by long-wave formation it performs oscillations around its maximum height while travelling at an almost constant speed (figure 6). This pattern conforms well with the phase-jump solution obtained by

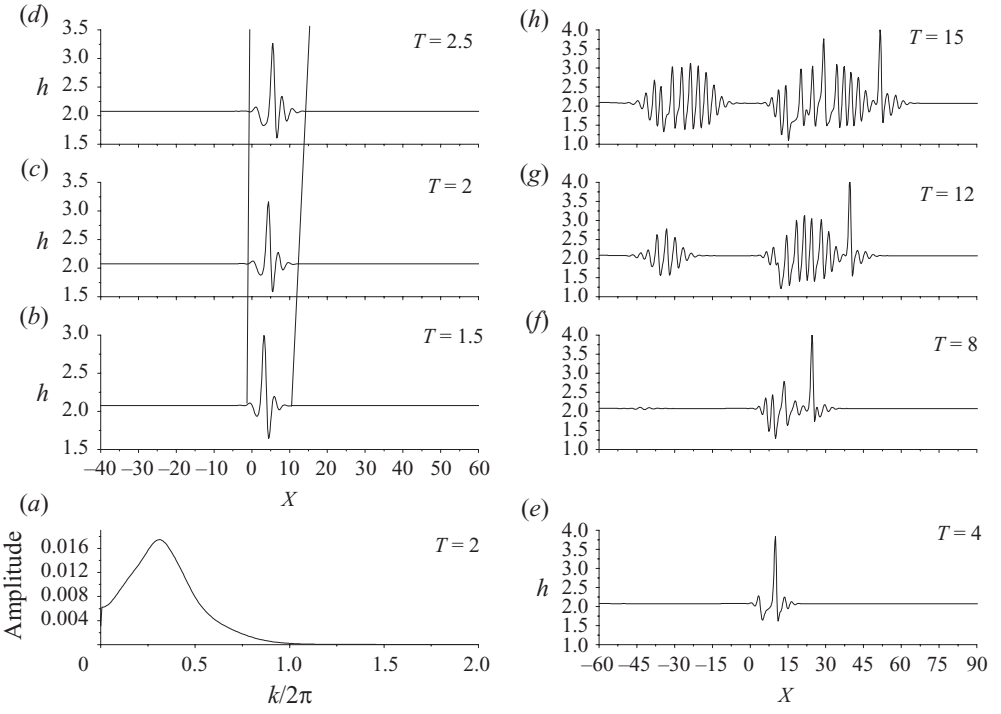

FIGURE 5. (*a*) Fourier transform and (*b–h*) snap-shots of interfacial waves for the air–deicing system in response to an impulsive disturbance; $H_0 = 2.07$, $\varepsilon = 0.5$, $x_0 = 0.8$, $We = 60$ and $Fr = 3.94 \times 10^4$.

Ma & Redekopp for their analysis describing short- to long-wave resonance of Stokes capillary–gravity waves (see also (3.23)).

Figure 6(*a–h*) illustrates the time evolution of the height and location of the major spike in the interfacial shape corresponding to figures 1, 2, 4 and 5. The capillary-wave formation is not identical in the final panels shown in the above figures, probably due to the oscillatory nature of the emerging phase-jump waveform and also due to the different time scales required to obtain such a wave depending on the initial amplitude. The heavy computational cost did not allow the simulations to proceed to significantly longer times than those depicted in figures 1, 2, 4 and 5. Nevertheless, the evolution of leading wave, as illustrated in figure 6, is quite indicative of the system dynamics and possesses very similar features. As can be gleaned from figure 6(*a*, *b*) the maximum film height after an initial transient exhibits a region of exponential growth followed by a region of almost constant height, indicating a tendency for saturation. The latter state, however, becomes unstable, leading to an oscillatory state of increased average height and a characteristic frequency that was seen to remain more or less the same as ε increased. It should be noted that the tendency for a steady waveform to appear that will eventually become unstable was mentioned in the analysis by Ma & Redekopp. The simulations performed here, especially for small amplitudes, indicate the path towards soliton formation via the destabilization of steady travelling waves, a pattern that was conjectured by the above authors. As ε increases (figure 6*c*, *d*), the region of wave saturation is bypassed and the system dynamics arrive at the state dominated by long waves immediately after the region of exponential growth. The final oscillatory state seems to be the same as far as the average height and frequency

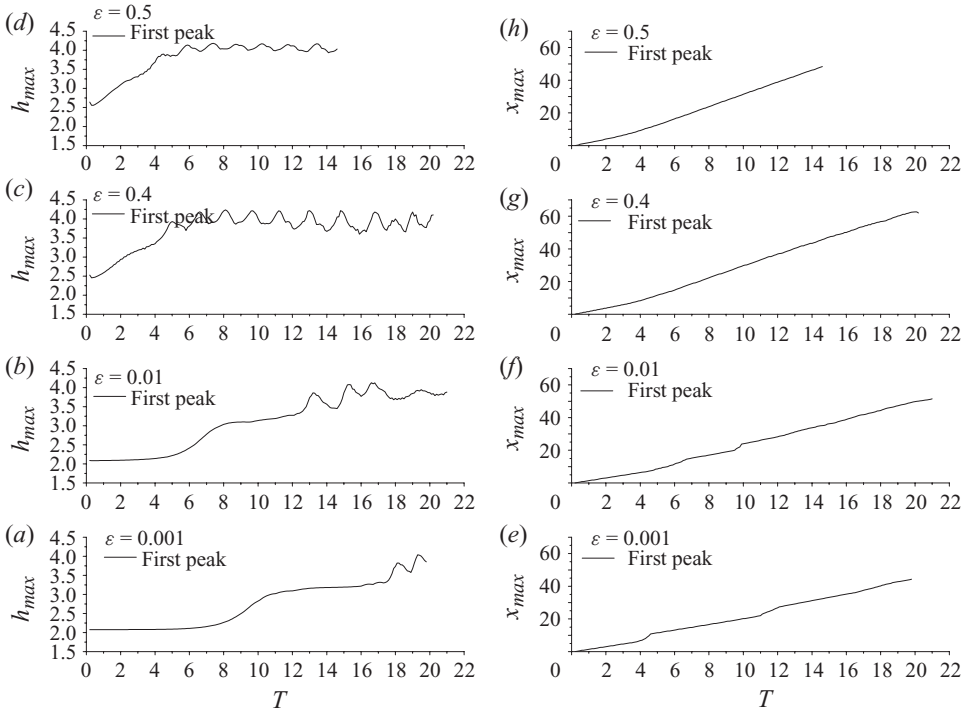

FIGURE 6. Evolution of the height and location of the leading peaks of interfacial waves for the air–deicing system when (*a*, *e*) $\varepsilon = 0.001$, (*b*, *f*) $\varepsilon = 0.01$, (*c*, *g*) $\varepsilon = 0.4$ and (*d*, *h*) $\varepsilon = 0.5$; $H_0 = 2.07$, $x_0 = 0.8$, $We = 60$ and $Fr = 3.94 \times 10^4$.

of oscillations are concerned. The interval of validity of linear theory decreases but still exists, as can be gleaned from the Fourier spectrum registered early on in the simulation (figures 4*a* and 5*a*) and the group velocity of the unstable wave (table 1 and figure 6*e–h*). The attributes of the wavepacket deviate from linearity due to the relatively small time interval from inception of the disturbance, but the pattern of wavepacket formation and translation, as predicted by linear theory, is present as well as its decomposition due to short- to long-wave resonance (figures 4 and 5). The initial group velocity as well as the wave speed of the final solitary wave can also be surmised by the initial and final slopes of the curves depicting the location of the leading spike versus time in figure 6(*e–h*). They follow a similar pattern with quite similar slopes during the time intervals of exponential growth and final solitary-wave transport. The former value can be cross-checked with the predictions of linear theory as it corresponds to the group velocity of the most unstable wave, C_G.

Decreasing *Fr* and *We*, which amounts to decreasing the film flow rate and increasing the interfacial surface tension, bears a stabilizing effect on interfacial waves, especially short ones. This can also be deduced by examining dispersion relation (3.2) and noting the $O(k^2)$ and $O(k^4)$ dependence of gravitational and capillary effects, respectively. The tendency for shorter waves to appear with increasing *We* is evident in the linear attributes of the emerging unstable wave (see also dispersion relation (3.2)), and this is also registered in the Fourier spectrum of the interface during the early stages of wave growth. Figures 4(*a*), 7(*f*) and 8(*f*) provide the dominant wavenumber at a time instant in that time interval, in agreement with the findings

	Linear theory ($We = 120$)	Numerical results ($We = 120$)	Linear theory ($We = 30$)	Numerical results ($We = 30$)
Wavelength	2.65	2.54	4.35	4.3
Period	1.5	1.45	2.8	2.75
C_G	2.35	2.4	2	2.1
C_{GL}	0.3	0.3	0.45	0.5
C_{GR}	4.7	4.6	3.8	3.7

TABLE 2. Attributes of the unstable wavepacket for interfacial waves of the air–deicing system predicted analytically via (3.2) and computed numerically; $x_0 = 0.8$, $H_0 = 2.076$ and $Fr = 3.94 \times 10^4$. C_G, C_{GL} and C_{GR} are defined in table 1.

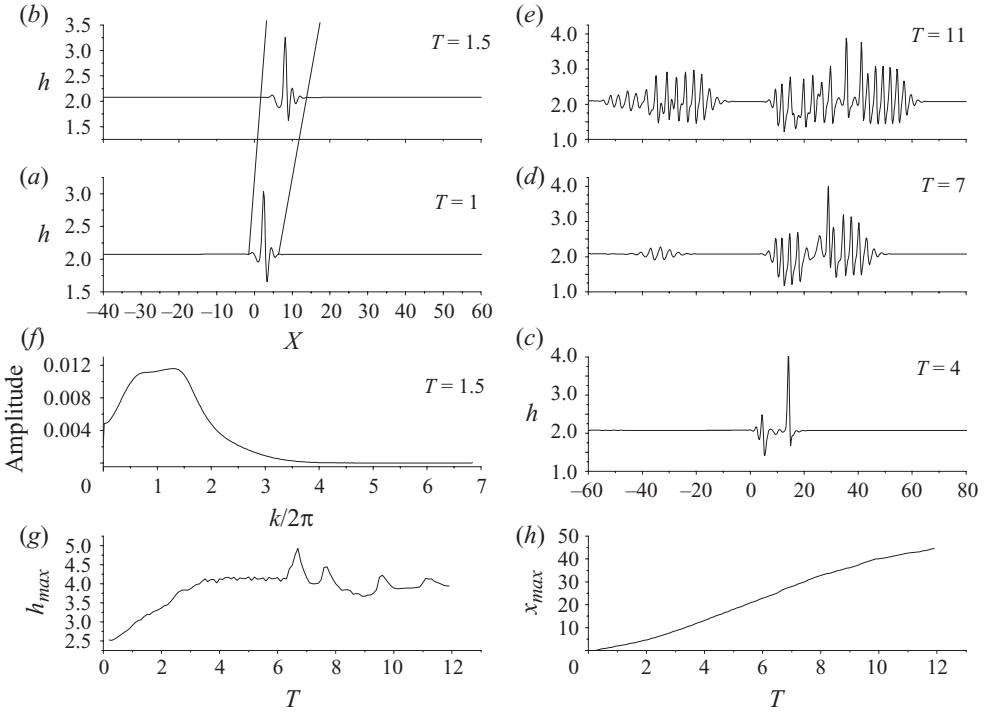

FIGURE 7. (*a–e*) Snap-shots, (*f*) Fourier transform and evolution of the (*g*) height and (*h*) location of the leading peaks of interfacial waves for the air–deicing system in response to an impulsive disturbance; $H_0 = 2.07$, $\varepsilon = 0.5$, $x_0 = 0.8$, $We = 120$ and $Fr = 3.94 \times 10^4$.

of linear theory. The relevant group velocities are also evaluated (table 2), and it is seen that the criterion $H_0\lambda \in (C_{GL}, C_{GR})$ is satisfied. Consequently, the pattern of resonance and long-wave formation is present while its onset is decelerated with increasing surface tension (figure 8). In addition, the waveform that appears due to the modulation of the long wave is affected by surface tension in a manner typical of soliton formation subject to varying *We*; see also the results reported by Meza & Balakotaiah (2008) for soliton formation in the context of falling films. Indeed, the wavelength of capillary waves ahead of the leading spike tends to decrease as *We* increases due to mitigation of the stabilizing effect of surface tension that allows for shorter waves to arise. The final panels of figures 5, 7 and 8 verify this tendency with

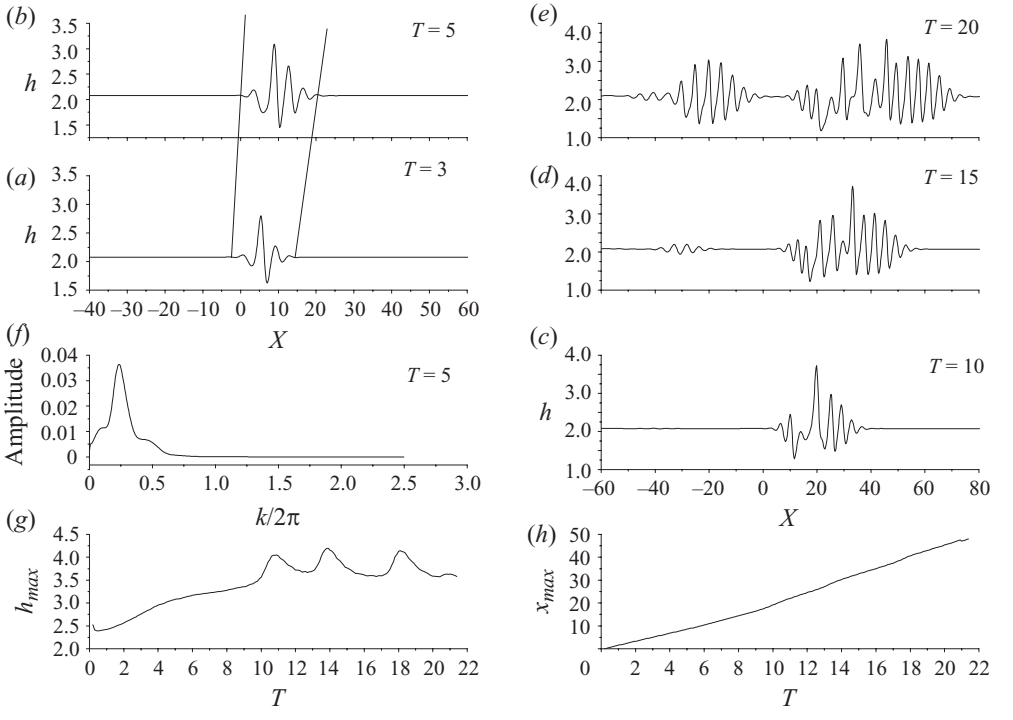

FIGURE 8. (*a–e*) Snap-shots, (*f*) Fourier transform and evolution of the (*g*) height and (*h*) location of the leading peaks of interfacial waves for the air–deicing system in response to an impulsive disturbance; $H_0 = 2.07$, $\varepsilon = 0.5$, $x_0 = 0.8$, $We = 30$ and $Fr = 3.94 \times 10^4$.

increasing *We* in the context of the present study. The final oscillatory state is also present in figures 7(*g*) and 8(*g*), following the initial growth of the maximum height, and is characterized by an increased period with increasing surface tension.

The above pattern persisted as long as parameter $\mathfrak{M}$ and product $H_0\lambda$ remained below a certain threshold value. Parameter $\mathfrak{M}$ sets the relative strength of viscous and inertia forces in the film whereas the product $H_0\lambda$ is a measure of the film velocity prescribed by the base flow. They both establish a parameter range below which an inertialess film flow can be assumed.

4.2. *Evolution of interfacial waves when film inertia is present*

In this section, the approach outlined above is adopted in order to interpret the findings of simulations for dynamic interaction of the air–water system. Figure 9 provides the dispersion relation for air–film systems in terms of ω_r and ω_i versus k_r graphs, when film inertia is important. Numerical analysis of the dispersion relation via the pinching method (Pelekasis & Tsamoopoulos 2001) reveals that the air–water system is absolutely unstable, i.e. C_{GL} is negative but still close to zero when compared against the group velocity of the most unstable wave (see also table 3). However, as *Fr* decreases the instability becomes convective, i.e. $C_{GL} > 0$, while criticality is reached for the *Fr* value of 6170, roughly. As already stressed in the previous sections the analysis carried out in § 3 is not valid for the case of water for which film inertia is important, and therefore (2.12) that describes the evolution of film thickness is not valid. However, it will be seen in the following that the mechanism of long- to

	Linear theory ($Fr = 9.2 \times 10^4$)	Numerical results ($Fr = 9.2 \times 10^4$)	Linear theory ($Fr = Fr_{Cr} = 6172$)	Linear theory ($Fr = 9259$)
Wavelength	3.85	3.9	5.2	4.1
Period	3.1	3	3.6	2.7
C_G	1.5	1.45	1.8	2

TABLE 3. Attributes of the unstable wavepacket for interfacial waves of the air–water system predicted via linear stability analysis by Pelekasis & Tsamopoulos (2001) and computed numerically; $x_0 = 1.5$, $\lambda = 0.27$, $H_0 = 3.326$, $We = 46$ and $H_0\lambda \approx 0.9$. C_G is defined in table 1.

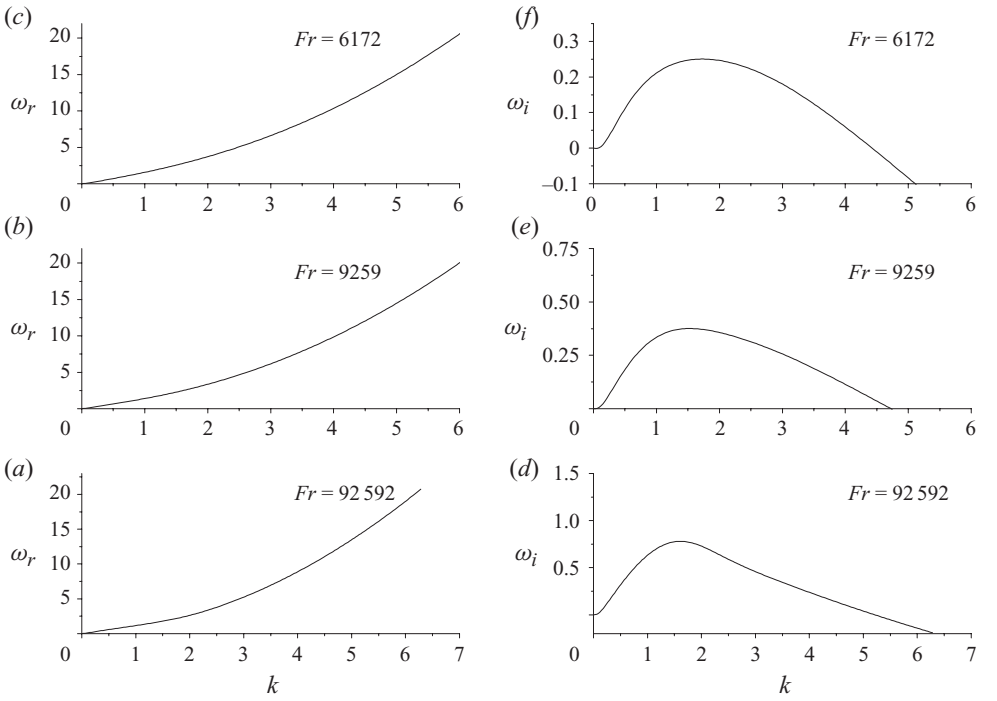

FIGURE 9. Dispersion relation, $\omega_r = \omega_r(k)$ and $\omega_i = \omega_i(k)$, corresponding to interfacial waves for the air–water system, when (*a*, *d*) $Fr = 6172$, (*b*, *e*) $Fr = 9259$ and (*c*, *f*) $Fr = 9.2 \times 10^4$; $H_0 = 3.326$, $x_0 = 1.5$ and $We = 46$.

short-wave resonance leading to soliton formation is quite useful in providing insight on the system dynamics.

Numerical tests around the region of critical Fr, with the rest of the parameters pertaining to the air–water system, revealed the same pattern of subcritical bifurcation previously discussed for the de-/anti-icing fluids. As Fr gradually increases this behaviour is recovered until a threshold value is reached, $Fr \approx 9260$, beyond which a wavepacket is formed that grows and translates with the characteristics of the linear wave. The instability is convectively unstable for $9260 \leqslant Fr < 37\,037$ and becomes absolutely unstable in the parameter range that is relevant to the air–water system, $Fr \sim 92\,000$. Figures 10–12 illustrate the dynamic response of the air–water system subject to an increasingly large amplitude of the initial impulsive disturbance. The response is distinctly different from that in the neighbourhood of critical Fr. In all

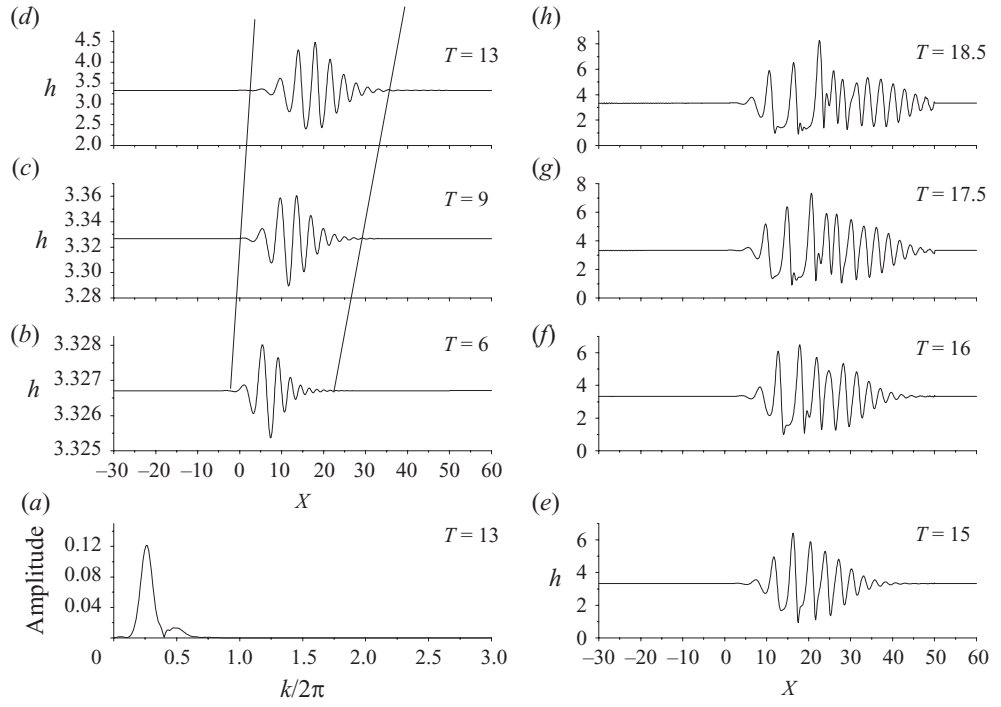

FIGURE 10. (*a*) Fourier transform and (*b–h*) snap-shots of interfacial waves for the air–water system in response to an impulsive disturbance; $H_0 = 3.326$, $\varepsilon = 0.0001$, $x_0 = 1.5$, $We = 46$ and $Fr = 9.2 \times 10^4$.

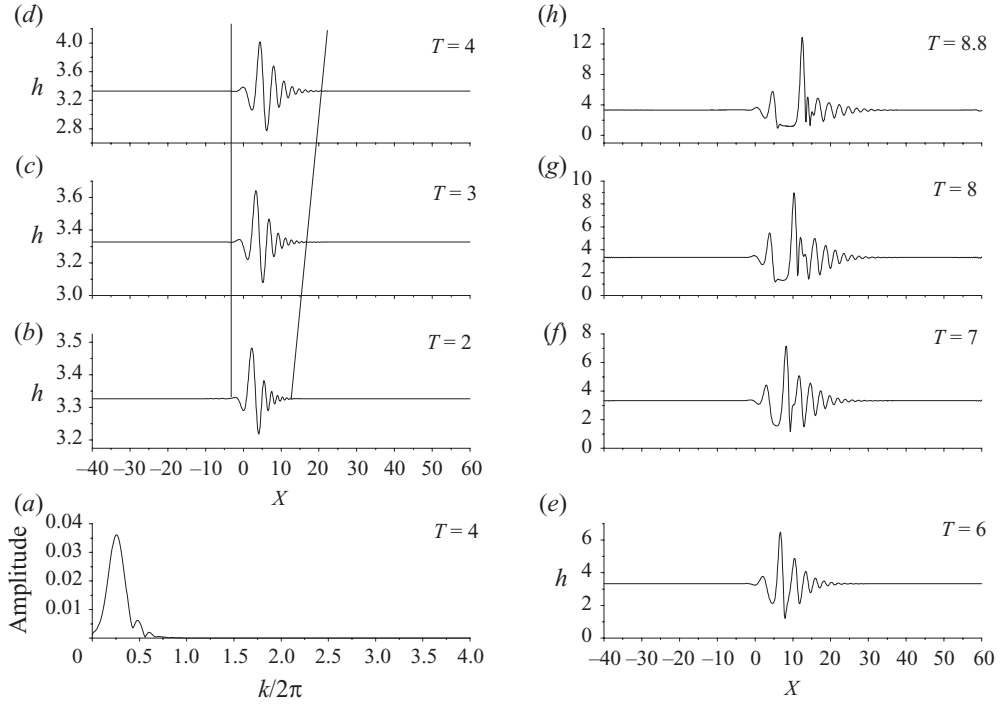

FIGURE 11. (*a*) Fourier transform and (*b–h*) snap-shots of interfacial waves for the air–water system in response to an impulsive disturbance; $H_0 = 3.326$, $\varepsilon = 0.1$, $x_0 = 1.5$, $We = 46$ and $Fr = 9.2 \times 10^4$.

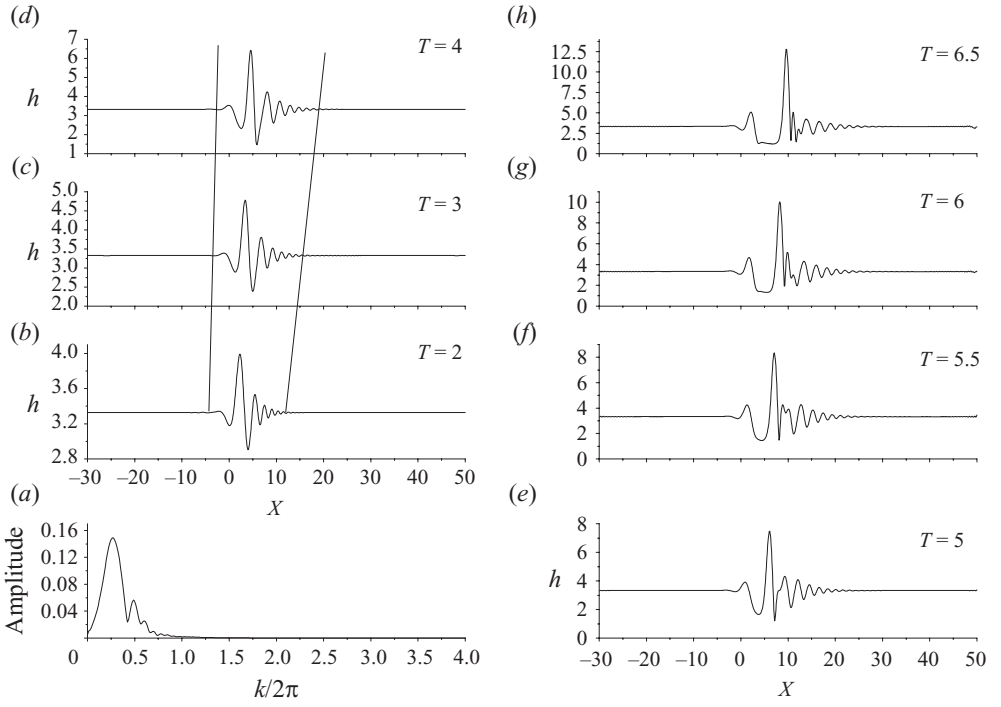

FIGURE 12. (*a*) Fourier transform and (*b–h*) snap-shots of interfacial waves for the air–water system in response to an impulsive disturbance; $H_0 = 3.326$, $\varepsilon = 0.4$, $x_0 = 1.5$, $We = 46$ and $Fr = 9.2 \times 10^4$.

cases a wavepacket consisting of the most unstable wave, $k_r = 1.6$, is formed, grows and translates in the manner predicted by linear theory (see also table 3). The group velocity of its left edge is close to zero but since the growth rate, $\omega_{0i} = 0.09$, of the absolutely unstable wave, $k_r = 1.4$, is very small compared to that of the most unstable wave, $\omega_{0i} = 0.78$, the response is dominated by the latter. As time elapses the evolution of the wavepacket deviates from linearity exhibiting spikes, while the spectrum is progressively enriched in the long-wave regime. The time over which this behaviour is evident decreases with increasing amplitude. Upon examination of the dispersion relation in the long-wave regime, $k \to 0$, the phase speed of long waves is $\omega/k \approx H_0\lambda$, which assumes the value $H_0\lambda \approx 0.9$ when $x_0 = 1.5$. This value is clearly within the interval of group velocities of the translating wavepacket. In fact, it is smaller than the group velocity of the most unstable wave, $C_G \approx 1.5$ for $k_r = 1.6$ from table 3, which probably explains why long waves first appear on the left side of the packet, as it is on this side that the short- to long-wave resonance criterion, $H_0\lambda = C_G$, is met. Once long waves appear the wavepacket is dominated by a single spike that keeps growing. A saturation height such as the one observed for anti-icing fluids was not observed for simulations with the water–air system, as long as the product $H_0\lambda$ remained above a certain threshold value. Based on the simulations that were performed when the location of the disturbance is at $x_0 = 0.8$, in which case $\lambda \approx 0.3$ from the Blasius solution, it was seen that when the mean film thickness H_0 is reduced from 1.4 to 0.7 the final wave pattern is changed from the one exhibiting a constantly growing spike to the saturated oscillatory spike obtained with anti-icing fluids. In other words the role of film inertia is heavily dependent on the characteristic interfacial velocity $H_0\lambda$ provided by the base flow.

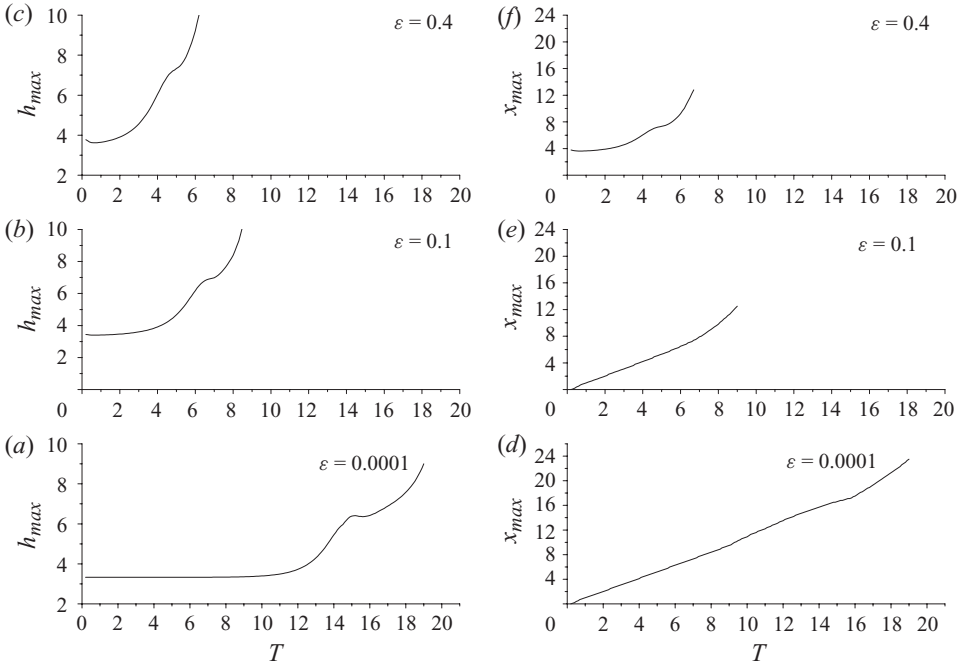

FIGURE 13. Evolution of the height and location of the leading peaks of interfacial waves for the air–water system when (*a*, *d*) $\varepsilon = 0.0001$, (*b*, *e*) $\varepsilon = 0.1$ and (*c*, *f*) $\varepsilon = 0.4$; $H_0 = 3.326$, $x = 1.5$, $We = 46$ and $Fr = 9.2 \times 10^4$.

Figure 13 illustrates the time evolution of the maximum height of the wavepacket as well as its position in space. They both exhibit a similar behaviour with de-/anti-icing fluids. More specifically, the maximum height is characterized by an initial transient followed by exponential growth, pertaining to the linear growth of the packet. This process is arrested by the onset of long waves, leading to spike formation and further growth. The speed of translation of the maximum can be inferred by the evolution of its location, which exhibits two regions, namely the one corresponding to linear growth, during which the speed is determined by that of the most unstable wave of the packet, and the one corresponding to spike formation and growth. The latter is larger and keeps increasing, and this conforms with the pattern of spike growth and soliton formation proposed for the case of anti-icing fluids.

At this point it should be stressed that simulations cannot proceed beyond a certain height of the growing spike, due to excessive growth of the displacement thickness that compromises the validity of the triple-deck theory. It is, however, conjectured here that what is captured by the simulations is indeed the root to solitary-wave formation, in a manner similar to the case of anti-icing fluids. However, due to film inertia, the saturation height for the case of water is expected to be much larger, thus rendering its accurate evaluation by the simulations very difficult, if not impossible, since the triple-deck structure may be destroyed long before soliton formation reaches saturation. Cusp formation as a result of a finite-time singularity was anticipated in studies of dynamic boundary-layer interaction with surface distortions (Brotherton-Ratcliffe & Smith 1987; Smith 1988), and we believe that this is reflected in the numerical results presented here in the form of spike formation, leading to finite-time singularities and cusps in the shape of the interface of water films. As was seen in

	Linear theory ($We = 92$)	Numerical results ($We = 92$)	Linear theory ($We = 23$)	Numerical results ($We = 23$)
Wavelength	2.95	3.1	5.2	5.2
Period	2.5	2.35	4.25	4.2
C_G	1.5	1.45	1.55	1.5

TABLE 4. Attributes of the unstable wavepacket for interfacial waves of the air–water system predicted via linear stability analysis by Pelekasis & Tsamopoulos (2001) and computed numerically; $x_0 = 1.5$, $H_0 = 3.326$ and $Fr = 9.2 \times 10^4$. C_G is defined in table 1.

the previous subsection, in the case of de-/anti-icing fluids film viscosity prevents the finite-time singularity from arising and produces oscillations around a saturation height that is roughly twice the base flow height H_0.

Close examination of the final panels in figures 10–12 further corroborates this interpretation. Indeed the shape of the interface is characterized by a spike that is preceded by a number of capillary waves and followed by a depression of the interface. In particular, when $\varepsilon = 0.1$ and 0.4, in which case the dynamics of the system evolve faster, the final panels in figures 11 and 12 indicate the tendency for the same solitary wave pattern to develop within a time interval that decreases as the amplitude of initial disturbance increases. Changing the *We* number while keeping the rest of the parameters the same as in figure 12 leads to a similar wave pattern consisting of the linear wavepacket growth and translation, the linear characteristics of the emerging wavepacket can be gleaned from Table 4, followed by spike formation and a solitary-wave-type arrangement (figures 14 and 15). The wavelength of the preceding capillary waves tends to decrease as the *We* number increases, or equivalently, as surface tension decreases and, consequently, its stabilizing effect on short waves attenuates. This is also typical behaviour of solitary-wave formation in the presence of capillary effects. The effect of film inertia has been recently studied for the case of a falling film by Meza & Balakotaiah (2008), who showed that a saturation height as large as 10-fold of the mean initial height can be achieved, when film inertia dominates over viscous and capillary effects.

5. Conclusions

Based on the above we can conclude on the mechanism that is responsible for the wave patterns that arise on a film–air interface in our triple-deck simulations, when the boundary layer drags the thin film. The research focuses on viscous films in which case the T–S waves that grow in the bulk of the boundary layer travel much faster than waves on the film–air interface, thus allowing for treatment of the flow in the gas phase as quasi-steady. For this flow arrangement and considering realistic fluids, such as water or de-/anti-icing fluids, the base flow, consisting of a shear flow in the film driven by a Blasius boundary layer in the gas phase, loses stability to interfacial waves. The latter translate and grow in the form of a wavepacket that is predicted by linear theory. The wavepacket never quite saturates. Rather it disintegrates due to energy being channelled to long waves that arise as a result of a short- to long-wave resonance. The latter is of the form first proposed by Djordjevic & Redekopp for Stokes capillary–gravity water waves, and occurs whenever the phase speed of long waves in the limit as $k \to 0$, i.e. $H_0\lambda$, falls within the interval determined by the left and right travelling waves of the advancing wavepacket, i.e. $C_{GL} < H_0\lambda < C_{GR}$. Weakly nonlinear analysis via the multiple-time-scale technique, which allows for interaction

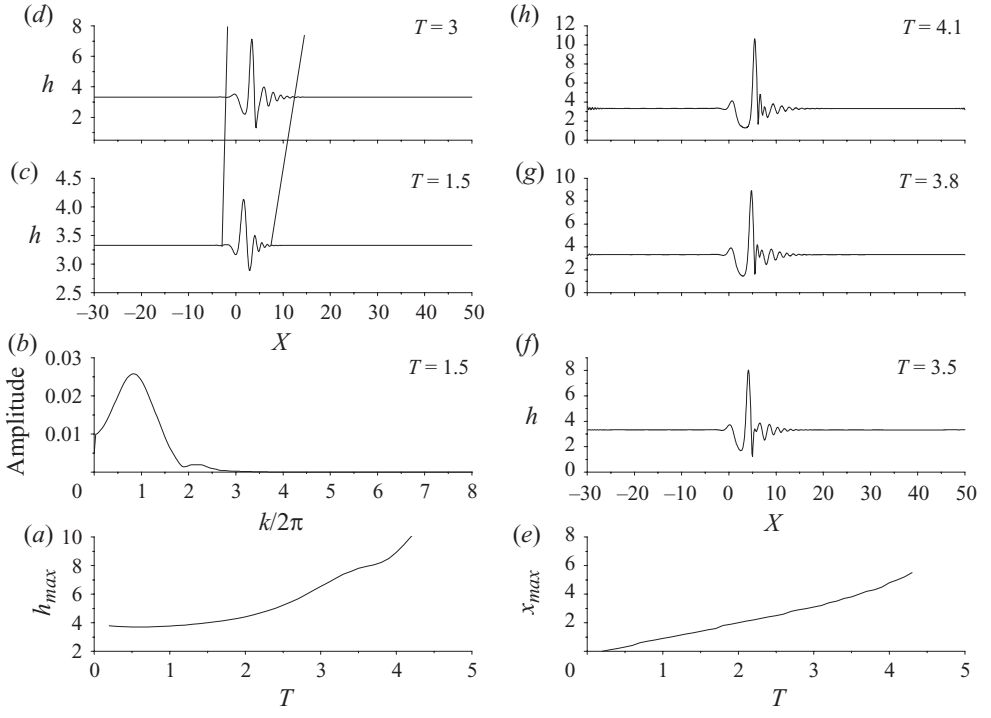

FIGURE 14. (*a–e*) Snap-shots, (*f*) Fourier transform and evolution of the (*g*) height and (*h*) location of the leading peaks of interfacial waves for the air–water system in response to an impulsive disturbance; $H_0 = 3.326$, $\varepsilon = 0.4$, $x_0 = 1.5$, $We = 92$ and $Fr = 9.2 \times 10^4$.

between the unstable interfacial wave and the mean-flow component, i.e. long waves, provides a Davey–Stewartson-type set of PDEs, describing the dynamics of the system that verifies the possibility for the above type of resonance for the problem under consideration. Numerical simulations conducted over a wide parameter range concur with this picture and also capture the final wave pattern that consists of solitons whose spikes travel faster than the original wavepacket while at the same time oscillating around a maximum value. The waveforms that were calculated resemble the phase-jump solution obtained by Ma & Redekopp for the set of equations describing short- to long-wave resonant interaction for Stokes capillary–gravity waves. It should be stressed that in the latter flow arrangement the short- to long-wave resonance occurs and becomes dominant as the liquid depth becomes much smaller than the wavelength of gravity waves. This pattern was fully captured for the case of de-/anti-icing fluids for which the weakly nonlinear analysis is valid. For the case of water–air system only the preliminary stages were captured, up to the deconstruction of the travelling wavepacket, leading to spike and soliton formation, without ever reaching a saturated spike height. This is due to the increased film inertia of water that leads to a much larger height of the emerging spike, to the point that the triple-deck formulation loses validity due to massive separation of the boundary layer. The collapse of the triple-deck flow arrangement in water films is manifested in the form of a finite-time singularity and cusp formation in the pressure gradient (see also the relevant graphs reported in I), in the manner described by Smith (1988) and Brotherton-Ratcliffe & Smith (1987) for flows over distorted boundaries via the interactive boundary-layer separation. In the case of de-/anti-icing fluids, film viscosity leads

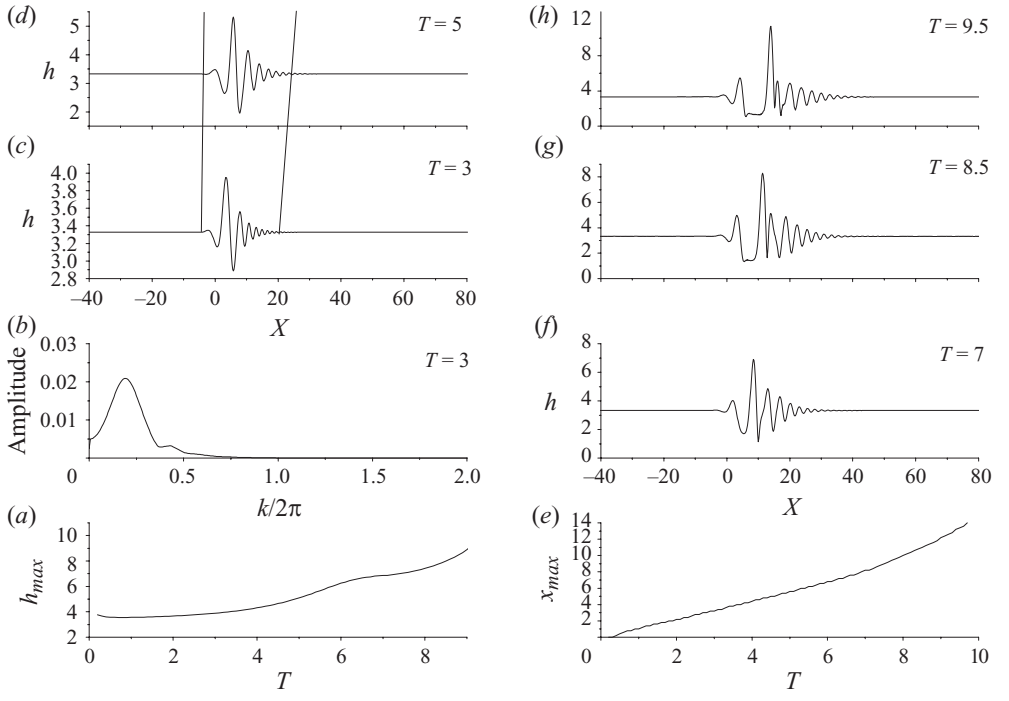

FIGURE 15. (*a–e*) Snap-shots, (*f*) Fourier transform and evolution of the (*g*) height and (*h*) location of the leading peaks of interfacial waves for the air–water system in response to an impulsive disturbance; $H_0 = 3.326$, $\varepsilon = 0.4$, $x_0 = 1.5$, $We = 23$ and $Fr = 9.2 \times 10^4$.

to solitary waves with maximum thickness that oscillates around a saturation height of $2H_0$.

The wave pattern obtained in the case of air–water systems is probably the wave identified by Craik (1966) as slow wave, whose speed was of the same order of magnitude as the velocity of the interface while its thickness exhibited steep spikes. The product $H_0\lambda$ is a measure of the interfacial speed and signifies the onset of short- to long-wave resonance with waves whose group velocity C_G is equal to the phase speed of long waves, $H_0\lambda$. Craik, in his analysis, emphasized the importance of Reynolds stresses in the onset of unstable interfacial waves. Weakly nonlinear analysis performed herein reveals that Reynolds stresses are essential for growth of long waves to occur to $O(\varepsilon^2)$, due to self-interaction of short waves, and destabilize the translating wavepacket.

A separation bubble is also present in the case of de-/anti-icing fluids without, however, reaching quite the extent of water spikes (see relevant graphs presented in I). This aspect of the solution may play a central role in the performance deterioration of airfoils under severe rainfall conditions. What remains to be seen in order to establish this mechanism is whether the above pattern will persist under three-dimensional disturbances. Clearly, formation of rivulets will take place, but the two-dimensional structure described above is expected to play a significant role in the onset of three-dimensional disturbances, given the speed of the emerging waves and the fact that solitons tend to be stable once they are formed, at many occasions. This dynamic pattern is supported by previous studies on the nonlinear stability of high-frequency

T–S waves. Such waves also emerge at supercritical conditions and are initially described by a generalized Schrodinger equation with a cubic nonlinearity (Smith 1986). Subsequently, their amplitude growth is controlled by the integral–differential Benjamin–Ono equation (Smith & Burggraf 1985), which was later seen (Li *et al.* 1998) to involve interaction between solitary waves and the originally emerging wavepacket, leading to finite-time singularities and cusp formation. In the same context, Kachanov *et al.* (1993) showed the connection between the Benjamin–Ono equation and solitary-wave formation and stressed the issue of spike formation and transition in boundary layers. They also verified the persistence of this process in the presence of three-dimensional disturbances, against available experimental observations.

Nevertheless, in the context of the present study, this is an issue that needs to be addressed in detail. Perhaps, derivation of a three-dimensional Davey–Stewartson-type of coupled PDEs via the three-dimensional triple-deck (Smith & Stewart 1987) description of the flow system under consideration is warranted for a more realistic representation. Incorporation of a forcing term will also be useful in order to model flow-control practices. Simulations conducted in the present study in the context of two-dimensional disturbances indicate that adding surfactants in the film may have a favourable effect, in the sense that they delay the onset of spike formation, as can be gleaned upon comparing figures 5, 7 and 8 for a de-icing film and figures 12, 14 and 15 for a water film.

M.V. wishes to acknowledge the scholarships 'PENED' of the Greek Secretariat of Research and 'PYTHAGORAS' of the Greek Ministry of Education for support during this work.

Appendix A

To leading order the linear stability analysis formulation is recovered:

$$\frac{\partial^4 \Phi_1}{\partial \overline{Y}^4} = \lambda \overline{Y} \frac{\partial^3 \Phi_1}{\partial \xi \partial \overline{Y}^2}, \tag{A 1}$$

$$\frac{\partial \Phi_1}{\partial \overline{Y}}(\overline{Y} \to \infty) = \lambda (A_1 + f_1), \tag{A 2}$$

$$\frac{\partial^2 \Phi_1}{\partial \overline{Y}^2}(\overline{Y} \to \infty) = 0, \tag{A 3}$$

$$\overline{Y} = 0: \quad \Phi_1 = \frac{\partial \Phi_1}{\partial \overline{Y}} = 0, \tag{A 4}$$

$$P_1 = \frac{1}{\pi} \int_{-\infty}^{+\infty} \frac{\partial A_1}{\partial s} \frac{\mathrm{d}s}{\xi - s}, \tag{A 5}$$

$$\overline{Y} = 0: \quad -C_p \frac{\partial f_1}{\partial \xi} = -\frac{H_0^2}{2} \frac{\partial^3 \Phi_1}{\partial \xi \partial \overline{Y}^2} - H_0 \lambda \frac{\partial f_1}{\partial \xi} + \frac{H_0^3}{3} \frac{\partial^2 P_1}{\partial \xi^2} + \frac{H_0^3}{3} \frac{(\rho_w/\rho - 1)}{Fr} \frac{\partial^2 f_1}{\partial \xi^2} - \frac{H_0^3}{3We} \frac{\partial^4 f_1}{\partial \xi^4}. \tag{A 6}$$

The solution of the above problem in terms of the transformed variable $z=\overline{Y}(\mathrm{i}\lambda k)^{1/3}$ reads

$$A_{1,1}=\frac{d(\zeta,\zeta_1,\tau)\lambda^2 Ai'(z=0)}{k(\mathrm{i}k\lambda)^{1/3}\displaystyle\int_0^\infty Ai(z)\,\mathrm{d}z-\lambda^2 Ai'(z=0)}=-d(\zeta,\zeta_1,\tau)\frac{3\lambda^2 0.259}{k(\mathrm{i}k\lambda)^{1/3}+3\lambda^2 0.259}, \quad (A\,7)$$

$$P_{1,1}=kA_{1,1}, \quad (A\,8)$$

$$\Phi_{11}=d\;C(k)\Phi(z)=d\frac{\lambda k}{k(\mathrm{i}k\lambda)^{1/3}+3\lambda^2 0.259}\left[3\int_\infty^z (zAi(s)-sAi(s))\,\mathrm{d}s+z-3\times 0.259\right]. \quad (A\,9)$$

In order to obtain the complex-conjugate solution we set $z=\overline{Y}(-\mathrm{i}k\lambda)^{1/3}$. The problem to order ε^2 reads as

$$\frac{\partial^4\Phi_2}{\partial\overline{Y}^4}=\lambda\overline{Y}\frac{\partial^3\Phi_2}{\partial\xi\,\partial\overline{Y}^2}+\frac{\partial\Phi_1}{\partial\overline{Y}}\frac{\partial^3\Phi_1}{\partial\xi\,\partial\overline{Y}^2}-\frac{\partial\Phi_1}{\partial\xi}\frac{\partial^3\Phi_1}{\partial\overline{Y}^3}+\lambda\overline{Y}\frac{\partial^3\Phi_1}{\partial\zeta\,\partial\overline{Y}^2}, \quad (A\,10)$$

$$\frac{\partial\Phi_2}{\partial\overline{Y}}(\overline{Y}\to\infty)=\lambda(A_2+f_2), \quad (A\,11)$$

$$\frac{\partial^2\Phi_2}{\partial\overline{Y}^2}(\overline{Y}\to\infty)=0, \quad (A\,12)$$

$$\overline{Y}=0:\quad \Phi_2=\frac{\partial\Phi_2}{\partial\overline{Y}}=0, \quad (A\,13)$$

$$P_2=\frac{1}{\pi}\int_{-\infty}^{+\infty}\left(\frac{\partial A_2}{\partial s}+\frac{\partial A_1}{\partial\zeta}\right)\frac{\mathrm{d}s}{\xi-s}, \quad (A\,14)$$

$$\overline{Y}=0:\quad -C_p\frac{\partial f_2}{\partial\xi}+\frac{H_0^2}{2}\frac{\partial^3\Phi_2}{\partial\xi\,\partial\overline{Y}^2}+H_0\lambda\frac{\partial f_2}{\partial\xi}-\frac{H_0^3}{3}\frac{\partial^2 P_2}{\partial\xi^2}-\frac{H_0^3}{3}\frac{1}{Fr}\frac{\partial^2 f_2}{\partial\xi^2}+\frac{H_0^3}{3We}\frac{\partial^4 f_2}{\partial\xi^4}-C_G\frac{\partial f_1}{\partial\zeta}=R_1+R_2, \quad (A\,15)$$

where R_1 represents linear terms involving derivatives with respect to slow space coordinate ζ and R_2 represents terms arising due to nonlinearity.

The mean flow, fundamental and second harmonic components of the solution are obtained via solution of the following problems.

A.1. *Mean-flow component*

$$\frac{\partial^4\Phi_{2,0}}{\partial\overline{Y}^4}=\mathrm{i}k\left[\frac{\partial\Phi_{1,-1}}{\partial\overline{Y}}\frac{\partial^2\Phi_{1,1}}{\partial\overline{Y}^2}-\frac{\partial\Phi_{1,1}}{\partial\overline{Y}}\frac{\partial^2\Phi_{1,-1}}{\partial\overline{Y}^2}+\frac{\partial^3\Phi_{1,1}}{\partial\overline{Y}^3}\Phi_{1,-1}-\frac{\partial^3\Phi_{1,-1}}{\partial\overline{Y}^3}\Phi_{1,1}\right], \quad (A\,16)$$

$$\overline{Y}\to\infty:\quad \Phi_{2,0}=\overline{Y}\lambda(A_{2,0}+f_{2,0}),\quad \overline{Y}=0:\quad \Phi_{2,0}=\frac{\partial\Phi_{2,0}}{\partial\overline{Y}}=0, \quad (A\,17a,b)$$

$$P_{2,0}=0. \quad (A\,18a,b)$$

A.2. *Fundamental component*

$$\frac{\partial^4\Phi_{2,1}}{\partial\overline{Y}^4}=\lambda\overline{Y}\frac{\partial^2\Phi_{2,1}}{\partial\overline{Y}^2}\mathrm{i}k+\lambda\overline{Y}C\frac{\partial^2\Phi}{\partial\overline{Y}^2}\frac{\partial d}{\partial\zeta}, \quad (A\,19)$$

$$\overline{Y}\to\infty:\quad \Phi_{2,1}=\overline{Y}\lambda(A_{2,1}+f_{2,1}),\quad \overline{Y}=0:\quad \Phi_{2,1}=\frac{\partial\Phi_{2,1}}{\partial\overline{Y}}=0, \tag{A 20a, b}$$

$$P_{2,1}=kA_{2,1}-\mathrm{i}\frac{\partial A_{1,1}}{\partial\zeta}, \tag{A 21}$$

$$\begin{aligned}-C_p f_{2,1}\mathrm{i}k+\frac{H_0^2}{2}\mathrm{i}k\frac{\partial^2\Phi_{2,1}}{\partial\overline{Y}^2}+H_0\lambda\mathrm{i}kf_{2,1}+\frac{k^2H_0^3}{3}P_{2,1}+\frac{H_0^3}{3}\frac{k^2}{Fr}f_{2,1}\\ +\frac{k^4H_0^3}{3We}f_{2,1}-C_G\frac{\partial d}{\partial\zeta}=-\frac{H_0^2}{2}\frac{\partial d}{\partial\zeta}\frac{\partial^2\Phi}{\partial\overline{Y}^2}C-H_0\lambda\frac{\partial d}{\partial\zeta}+\frac{2H_0^3}{3}\mathrm{i}kP\frac{\partial d}{\partial\zeta}\\ -(\mathrm{i}k)^3\frac{4H_0^3}{3We}\frac{\partial d}{\partial\zeta}+\frac{2H_0^3}{3}\frac{\mathrm{i}k}{Fr}\frac{\partial d}{\partial\zeta}.\end{aligned} \tag{A 22}$$

A.3. *Second-harmonic component*

$$\frac{\partial^4\Phi_{2,2}}{\partial\overline{Y}^4}=\lambda\overline{Y}\frac{\partial^2\Phi_{2,2}}{\partial\overline{Y}^2}2\mathrm{i}k+\mathrm{i}kd^2C^2\left(\frac{\mathrm{d}^2\Phi}{\mathrm{d}\overline{Y}^2}\frac{\mathrm{d}\Phi}{\mathrm{d}\overline{Y}}-\Phi\frac{\mathrm{d}^3\Phi}{\mathrm{d}\overline{Y}^3}\right), \tag{A 23}$$

$$\overline{Y}\to\infty:\quad \Phi_{2,2}=\overline{Y}\lambda(A_{2,2}+f_{2,2}),\quad \overline{Y}=0:\quad \Phi_{2,2}=\frac{\partial\Phi_{2,2}}{\partial\overline{Y}}=0, \tag{A 24a, b}$$

$$P_{2,2}=2kA_{2,2}, \tag{A 25}$$

$$\begin{aligned}-C_p f_{2,2}2\mathrm{i}k+\frac{H_0^2}{2}2\mathrm{i}k\frac{\partial^2\Phi_{2,2}}{\partial\overline{Y}^2}+H_0\lambda2\mathrm{i}kf_{2,2}+\frac{(2k)^2H_0^3}{3}P_{2,2}+\frac{H_0^3}{3}\frac{(2k)^2}{Fr}f_{2,2}\\ +\frac{(2k)^4H_0^3}{3We}f_{2,2}=-(2\mathrm{i}k)d^2\left(H_0C\frac{\mathrm{d}^2\Phi}{\mathrm{d}\overline{Y}^2}+\frac{\lambda}{2}\right)+(2\mathrm{i}k)d^2\left(H_0^2\mathrm{i}kP\right)\\ -(2\mathrm{i}k)d^2\left(\frac{H_0^2}{We}(\mathrm{i}k)^3\right)+(2\mathrm{i}k)d^2\left(\frac{H_0^2}{Fr}\mathrm{i}k\right),\end{aligned} \tag{A 26}$$

and similarly for the complex-conjugate quantities.

The fundamental component of the $O(\varepsilon^3)$ problem satisfies the following set of equations:

$$\begin{aligned}\frac{\partial^4\Phi_{3,1}}{\partial\overline{Y}^4}-\lambda\overline{Y}\frac{\partial^2\Phi_{3,1}}{\partial\overline{Y}^2}\mathrm{i}k=\lambda\overline{Y}\frac{\partial^3\Phi_{2,1}}{\partial\zeta\partial\overline{Y}^2}+\lambda\overline{Y}\frac{\partial^3\Phi_{1,1}}{\partial\zeta_1\partial\overline{Y}^2}+2\mathrm{i}k\frac{\partial\Phi_{1,-1}}{\partial\overline{Y}}\frac{\partial^2\Phi_{2,2}}{\partial\overline{Y}^2}\\ -\mathrm{i}k\frac{\partial\Phi_{2,2}}{\partial\overline{Y}}\frac{\partial^2\Phi_{1,-1}}{\partial\overline{Y}^2}-2\mathrm{i}k\Phi_{2,2}\frac{\partial^3\Phi_{1,-1}}{\partial\overline{Y}^3}+\mathrm{i}k\Phi_{1,-1}\frac{\partial^3\Phi_{2,2}}{\partial\overline{Y}^3},\end{aligned} \tag{A 27}$$

$$\overline{Y}\to\infty:\quad \Phi_{3,1}=\overline{Y}\lambda(A_{3,1}+f_{3,1}),\quad \overline{Y}=0:\quad \Phi_{3,1}=\frac{\partial\Phi_{3,1}}{\partial\overline{Y}}=0, \tag{A 28a, b}$$

$$P_{3,1}=kA_{3,1}-\mathrm{i}\frac{\partial A_{2,1}}{\partial\zeta}-\mathrm{i}\frac{\partial A_{1,1}}{\partial\zeta_1}, \tag{A 29}$$

$$-C_p f_{3,1}\mathrm{i}k-C_G\frac{\partial f_{2,1}}{\partial\zeta}+\frac{\partial f_{2,1}}{\partial\tau}+f_{1,1}\omega_i'-C_G\frac{\partial d}{\partial\zeta_1}=R_L+R_{NL}+R_{01}, \tag{A 30}$$

and similarly for the complex-conjugate quantities. The parameter $\omega_i\equiv\varepsilon^2\omega_i'=O(\varepsilon^2)$ near criticality and consequently the time derivative of the term $\mathrm{e}^{\omega_i t}\approx\mathrm{e}^{\omega_i'\varepsilon^2 t}=\mathrm{e}^{\omega_i'\tau}$, signifying that linear growth contributes to $O(\varepsilon^3)$. Linear and nonlinear terms on

the left-hand side of (A 30) are grouped in R_L and R_{NL}, respectively, whereas terms arising as a result of interaction between the fundamental and mean-flow components are grouped in R_{01}. Equations (A 29) and (A 30) admit a solution of the form

$$f_{3,1} = e - \frac{\partial d}{\partial \zeta_1} C \frac{15\lambda 0.259\mathrm{i}(\mathrm{i}k\lambda)^{2/3} - k^2}{3k^2(\mathrm{i}k\lambda)^{2/3}} + \frac{\partial \alpha}{\partial \zeta} \frac{\mathrm{i}\lambda k}{(\mathrm{i}k\lambda)^{1/3}k + 3\lambda^2 0.259} \frac{15\lambda^2 0.259 + k(\mathrm{i}k\lambda)^{1/3}}{3k^2\lambda}$$
$$+ \frac{\partial^2 d}{\partial \zeta^2} \frac{\mathrm{i}2C}{9k} \frac{k - 90\lambda 0.259(\mathrm{i}k\lambda)^{1/3}}{k^2(\mathrm{i}k\lambda)^{1/3}} + \frac{|d|^2 d}{\lambda(\mathrm{i}k\lambda)^{1/3}} \left[\int_0^\infty \Psi_{3,1,P}\, \mathrm{d}\tau + \frac{\lambda^2}{k(\mathrm{i}k\lambda)^{1/3}} \int_0^\infty \Psi_{3,1,P}\tau\, \mathrm{d}\tau \right.$$
$$\left. + \frac{C^*(-\mathrm{i}k\lambda)^{1/3}}{2^{1/3}k} \left(\frac{b'}{3} + \int_0^\infty \Psi_{2,1,P}\, \mathrm{d}\tau \right) \right], \quad b' = b/d^2, \tag{A 31}$$

and similarly for the complex conjugate; e is an as yet undetermined constant and $\Psi_{3,1,P}(z)$ is the particular solution of the equation governing variations of the stream function to $O(\varepsilon^3)$. Similar solutions are obtained for the rest of the unknowns.

As can be gleaned from (A 30) the coefficient of the second-order component of the mean flow, $f_{2,0}$, participates in the dynamics of the fundamental component $f_{3,1}$. However, the former component, $f_{2,0}$, is left undetermined in the context of the $O(\varepsilon^2)$ problem. Focusing on the evolution equation of the interface to $O(\varepsilon^3)$ and isolating terms concerning the mean flow E°, we obtain the following relation:

$$(H_0\lambda - C_G)\frac{\partial f_{2,0}}{\partial \zeta} = -\frac{H_0^2}{2}\frac{\partial^3 \Phi_{2,0}}{\partial \zeta\, \partial \overline{Y}^2} + H_0^2 \left[f_{1,1}\frac{\partial P_{1,-1}}{\partial \zeta} + f_{1,-1}\frac{\partial P_{1,1}}{\partial \zeta} \right] - \frac{H_0^2}{We}\frac{\partial}{\partial \zeta}[(\mathrm{i}k)^3 f_{1,1} f_{1,-1}$$
$$+ (-\mathrm{i}k)^3 f_{1,1} f_{1,-1}] + \frac{H_0^2}{Fr}\frac{\partial}{\partial \zeta}[(-\mathrm{i}k) f_{1,1} f_{1,-1} + (\mathrm{i}k) f_{1,1} f_{1,-1}], \tag{A 32}$$

which involves only first- and second-order quantities and serves to determine $f_{2,0}$ and d along with (A 30).

REFERENCES

Bender, C. M. & Orszag. S. A. 1978 *Advanced Mathematical Methods for Scientists and Engineers.* McGraw-Hill.

Benjamin, T. B. 1961 The development of three dimensional disturbances in an unstable film of liquid flowing down in an inclined plane. *J. Fluid Mech.* **10**, 401.

Bezos, G. M., Dunham, R. E., Genry, G. L. & Melson, W. E. 1992 Wind tunnel aerodynamic characteristics of a transport-type airfoil in a simulated heavy rain environment. *Tech. Paper* 3184. NASA.

Blennerhassett, P. J. 1980 On the generation of waves by wind. *Phil. Trans. R. Soc. Lond.* A **298**, 451–494.

Brevdo, L., Laure, P., Dias, F. & Bridges, T. J. 1999 Linear pulse structure and signalling in a film flow on an inclined plane. *J. Fluid Mech.* **396**, 37–71.

Brotherton-Ratcliffe, R. V. & Smith, F. T. 1987 Complete breakdown of an unsteady interactive boundary layer (over a surface distortion or in a liquid layer). *Mathematika* **34**, 86–100.

Clamond, D. & Germain, J. P. 1999 Interaction between a Stokes wave packet and a solitary wave. *Eur. J. Mech.* B/*Fluids* **18** (1), 67–91.

Couairon, A. & Chomaz, J. 1997 Absolute and convective instabilities, front velocities and global modes in non-linear systems. *Physica* D **108**, 236–276.

Craik, A. D. D. 1966 Wind generated waves in thin liquid films. *J. Fluid Mech.* **26** (2), 369–392.

Craik, A. D. D. 1985 *Wave Interactions and Fluid Flows.* Cambridge University Press.

Davey, A., Hocking, L. M. & Stewartson, K. 1974 On the nonlinear evolution of three-dimensional disturbances in plane Poiseuille flow. *J. Fluid Mech.* **63**, 529–536.

Davey, A. & Stewartson, K. 1974 On three dimensional packets of surface waves. *Proc. R. Soc. Lond.* A **388**, 101.

Djordjevic, V. D. & Rdecopp, L. G. 1977 On two dimensional packets of capillary–gravity waves. *J. Fluid Mech.* **160**, 465–498.

Hill, E. G. & Zierten, T. A. 1993 Aerodynamic effects of aircraft ground deicing/anti-icing fluids. *J. Aircr.* **30**, 24.

Huerre, P. & Monkewitz, P. A. 1990 Local and global instabilities in spatially developing flows. *J. Fluid Mech.* **22**, 473–537.

Kachanov, Y. S., Ryzhov, O. R. & Smith, F. T. 1993 Formation of solitons in transitional boundary layers: theory and experiment. *J. Fluid Mech.* **251**, 273–297.

Li, L., Walker, J. D. A., Bowles, R. I. & Smith, F. T. 1998 Short-scale break-up in unsteady interactive layers: local development of normal pressure gradients and vortex wind-up. *J. Fluid Mech.* **374**, 335–378.

Lin, S. P. 1974 Finite amplitude side-band stability of a viscous film. *J. Fluid Mech.* **63** (3), 417–429.

Ludwieg, H. & Hornung, H. 1989 The instability of a liquid film on a wall exposed to an air flow. *J. Fluid Mech.* **200**, 217–233.

Ma, Y.-C. & Redekopp, L. G. 1979 Some solutions pertaining to the resonant interaction of long and short waves. *Phys. Fluids* **22** (10), 1872–1876.

Meza, C. E. & Balakotaiah, V. 2008 Modeling and experimental studies of large amplitude waves on vertically falling films. *Chem. Engng Sci.* **63**, 4704–4734.

Nelson, J. J., Alving, A. E. & Joseph, D. D. 1995 Boundary layer flow of air over water on a flat plate. *J. Fluid Mech.* **284**, 159–169.

Ozgen, S., Carbonaro, M. & Sarma, G. S. R. 2002 Experimental study of wave characteristics on a thin layer of de-/anti-icing fluid. *Phys. Fluids* **14**, 3391–3402.

Ozgen, S., Degrez, G. & Sarma, G. S. R. 1998 Two-fluid boundary layer stability. *Phys. Fluids* **10** (11), 2746–2757.

Pelekasis, N. A. & Tsamopoulos, J. A. 2001 Linear stability analysis of a gas boundary layer flowing past a thin liquid film over a flat plate. *J. Fluid Mech.* **436**, 321–352.

Rothmayer, A. P., Matheis, B. D. & Timoshin, S. N. 2002 Thin liquid films flowing over external aerodynamic surfaces. *J. Engng Math.* **42**, 341–357.

Saarlos, W. & Hohenberg, P. C. 1992 Fronts, pulses, sources and sinks in generalized complex Ginzburg–Landau equations. *Physica* D **56**, 303–367.

Smith, F. T. 1979 Nonlinear stability of boundary layers for disturbances of various sizes. *Proc. R. Soc. Lond.* A **368**, 573–589.

Smith, F. T. 1986 Two-dimensional disturbance travel, growth and spreading in boundary layers. *J. Fluid Mech.* **169**, 353–377.

Smith, F. T. 1988 Finite-time break-up can occur in any unsteady interacting boundary layer. *Mathematika* **35**, 256–273.

Smith, F. T. & Burggraf, O. R. 1985 On the development of large-sized short-scaled disturbances in boundary layers. *Proc. R. Soc. Lond.* A **399**, 25–55.

Smith, F. T. & Stewart, P. A. 1987 The resonant–triad interaction in boundary-layer transition. *J. Fluid Mech.* **179**, 227–252.

Smyrnaios, D. N., Pelekasis, N. A. & Tsamopoulos, I. A. 2000 Boundary layer flow of air past solid surfaces in the presence of rainfall. *J. Fluid Mech.* **425**, 79–110.

Stewartson, K. & Stuart, J. T. 1971 A non-linear instability theory for a wave system in plane Poiseuille flow. *J. Fluid Mech.* **48** (3), 529–545.

Timoshin, S. N. 1997 Instabilities in a high-Reynolds-number boundary layer on a film-coated surface. *J. Fluid Mech.* **353**, 163–195.

Timoshin, S. N. & Smith, F. T. 2003 Non-local interactions and feedback instability in a high Reynolds number flow. *Theor. Comput. Fluid Dyn.* **17**, 1–18.

Vlachomitrou, M. & Pelekasis, N. 2009 Nonlinear interaction between a boundary layer and a liquid film. *J. Fluid Mech.* **638**, 199–242.

Yiantsios, S. G. & Higgins, B. G. 1988 Linear stability of plane Poiseuille flow of two superposed fluids. *Phys. Fluids* **31**, 3225.